CrossMark

Wide-band Timing of the Parkes Pulsar Timing Array UWL Data

Małgorzata Curyło[1] , Timothy T. Pennucci[2] , Matthew Bailes[3,4] , N. D. Ramesh Bhat[5] , Andrew D. Cameron[3,4] ,
Shi Dai[6,7] , George Hobbs[7], Agastya Kapur[7,8], Richard N. Manchester[7] , Rami Mandow[7,8], Matthew T. Miles[3,4] ,
Christopher J. Russell[7], Daniel J. Reardon[3,4] , Ryan M. Shannon[3,4] , Renée Spiewak[3,9] , Willem van Straten[10] ,
Xing-Jiang Zhu[11] , and Andrew Zic[7,8]
[1] Astronomical Observatory, University of Warsaw, Aleje Ujazdowskie 4, 00-478 Warsaw, Poland; mcurylo@astrouw.edu.pl
[2] Institute of Physics, Eötvös Loránd University, Pázmány P.s. 1/A, 1117 Budapest, Hungary
[3] Centre for Astrophysics and Supercomputing, Swinburne University of Technology, PO Box 218, Hawthorn, Victoria 3122, Australia
[4] Australian Research Council Centre of Excellence for Gravitational Wave Discovery (OzGrav), Mail H29, Swinburne University of Technology, PO Box 218,
Hawthorn, VIC 3122, Australia
[5] International Centre for Radio Astronomy Research, Curtin University, Bentley, WA 6102, Australia
[6] School of Science, Western Sydney University, Locked Bag 1797, Penrith, NSW 2751, Australia
[7] Australia Telescope National Facility, CSIRO, Space and Astronomy, PO Box 76, Epping, NSW 1710, Australia
[8] Department of Physics and Astronomy and MQ Research Centre in Astronomy, Astrophysics and Astrophotonics, Macquarie University, NSW 2109, Australia
[9] Jodrell Bank Centre for Astrophysics, School of Physics and Astronomy, The University of Manchester, Manchester, M13 9PL, UK
[10] Institute for Radio Astronomy, and Space Research, Auckland University of Technology, Private Bag 92006, Auckland 1142, New Zealand
[11] Advanced Institute of Natural Sciences, Beijing Normal University, Zhuhai 519087, People's Republic of China

Abstract

In 2018 an ultra–wide-bandwidth low-frequency (UWL) receiver was installed on the 64 m Parkes Radio Telescope, enabling observations with an instantaneous frequency coverage from 704 to 4032 MHz. Here we present the analysis of a 3 yr data set of 35 ms pulsars observed with the UWL by the Parkes Pulsar Timing Array, using wide-band timing methods. The two key differences compared to typical narrowband methods are (1) generation of two-dimensional templates accounting for pulse shape evolution with frequency and (2) simultaneous measurements of the pulse time of arrival (TOA) and dispersion measure (DM). This is the first time that wide-band timing has been applied to a uniform data set collected with a single large fractional bandwidth receiver, for which such techniques were originally developed. As a result of our study, we present a set of profile evolution models and new timing solutions, including initial noise analysis. Precision of our TOA and DM measurements is in the range of 0.005–2.08 μs and $(0.043–14.24) \times 10^{-4}$ cm^{-3} pc, respectively, with 94% of the pulsars achieving a median TOA uncertainty of less than 1 μs.

Unified Astronomy Thesaurus concepts: Pulsar timing method (1305); Millisecond pulsars (1062)

1. Introduction

Pulsar timing array (PTA) experiments provide extraordinary means to study a wide range of physical phenomena across nearly all branches of physics and astronomy. These include characteristics of neutron stars themselves but can also relate to solar system dynamics, general relativity, or nanohertz gravitational waves (GWs) generated by various processes, such as supermassive black hole inspirals or cosmic strings (e.g., Burke-Spolaor et al. 2019; Vallisneri et al. 2020). However, as all of the above processes may have a very subtle effect on timing measurements (of the order of several nanoseconds), an increase of the precision and accuracy is a vital element of current PTA efforts. The three major pillars of PTA, working under a joint venture as the International Pulsar Timing Array (IPTA; Manchester & IPTA 2013), are the European Pulsar Timing Array (EPTA; Desvignes et al. 2016), the North American Nanoherthz Observatory for Gravitational waves (NANOGrav; McLaughlin 2013), and the Parkes Pulsar Timing Array (PPTA; Hobbs 2013). They have also been recently joined by the Indian Pulsar Timing Array (InPTA; Paul et al. 2019; Tarafdar et al. 2022) and are supported by the

Chinese Pulsar Timing Array (CPTA; Lee 2016) and the MeerKAT Pulsar Timing Array (MPTA; Miles et al. 2023).

There are a number of possible improvements that can be applied to observational strategies, instrumentation, and analysis techniques, such as increasing the number of pulsars in the array and the cadence of observations, or enlarging telescope apertures. In particular, several recent projects and facilities, such as the Five Hundred Meter Aperture Spherical Telescope (FAST; Hobbs et al. 2019) and the Canadian Hydrogen Intensity Mapping Experiment (CHIME/Pulsar Project; Amiri et al. 2021, 2022), will soon join PTA efforts and significantly increase available observing time and collecting area.

Another approach is to utilize wide-band receivers. In the first instance, the uncertainty of a timing measurement σ depends on the observing system and is described by the radiometer equation (Lorimer & Kramer 2004):

$$\sigma \propto \frac{T_{\mathrm{sys}}}{A_{\mathrm{eff}}}(\tau \Delta f)^{1/2}, \qquad (1)$$

where T_{sys} is the system's temperature, A_{eff} is the effective aperture, τ is the integration time, and Δf is the bandwidth. Apart from improvements based on Equation (1), wide-band receivers will also significantly broaden our capabilities of studying processes related to the interstellar medium (ISM), such as scintillation and dispersion measure (DM) variability. Currently, there are two telescopes with large instantaneous frequency

coverage used for PTA observations: the Effelsberg 100 m telescope with a 600–3000 MHz ultra-broadband (UBB) receiver,[12] and the Parkes Radio Telescope (Murriyang) with an ultra–wide-bandwidth low-frequency (UWL) receiver covering the largest frequency range of 704−4032 MHz (Hobbs et al. 2020). Installation of a new wide-band receiver is also planned for MeerKAT (Kramer et al. 2016), and the ultra–wide-band (UWB) feed at the Green Bank Telescope used by NANOGrav has recently entered a commissioning phase (Bulatek & White 2020).

In order to fully benefit from wide-band observations, it is important to adjust current analysis techniques. Growing apertures, observation time, and frequency coverage will significantly increase computational requirements, making processing of long PTA data sets arduous. Moreover, as many millisecond pulsars exhibit an intrinsic profile evolution with frequency, pulse shape can change drastically between the extreme ends of the band. These two effects, known collectively as the *large bandwidth problem*, are the main factors driving the development of new wide-band timing methods.

In general, the procedure of timing analysis consists of measuring the observed pulse times of arrival (TOAs) via the template-matching technique, which are then compared with the timing model. The model is supposed to accurately predict the periodicity of the pulsar's radio emission, fitting for parameters such as spin period and its derivative, position, and proper motion, or binary parameters if applicable. Differences between the observations and the model (the residuals) may manifest as either white or red noise (systematic and time correlated, respectively). In the former case, the main contributors are radiometer noise and jitter (Helfand et al. 1975; Shannon et al. 2014), while for the latter these could be pulsar intrinsic spin noise (Shannon & Cordes 2010), DM variations, or GWs. In other words, the sensitivity of the PTA depends on the accuracy of both the TOA measurement (and hence on the template used) and timing solutions, including a proper characterization of noise sources.

Typically, template matching is performed using a frequency-averaged profile template that will deviate from the true pulse shape at different frequencies. In order to mitigate this problem, it is common to divide the band and measure the so-called subbanded TOAs with one average template per subband and/or use additional parameters in the timing model (frequency-dependent (FD) parameters). The wide-band timing techniques (presented by Pennucci et al. 2014; Liu et al. 2014) offer an elegant and more direct solution by generation of a two-dimensional profile template maintaining frequency resolution (model of the profile evolution) and a simultaneous measurement of one TOA and DM at a reference frequency for the whole band. In particular, wide-band timing methods from Pennucci et al. (2014) were applied to the 12.5 yr data set from NANOGrav (Alam et al. 2021b, hereafter NG12.5) and directly compared with a corresponding narrowband release (Alam et al. 2021a). It was shown that the number of TOAs was reduced by a factor of 33, while maintaining a similar level of precision in terms of timing model and noise parameters (at least 2σ agreement). NG12.5 have also reported improvement of timing results by 10%–15% for pulsars that were impaired by stronger environmental effects such as high DM and scintillation. Similarly, Nobleson et al. (2022) presented a wide-band analysis of five pulsars observed with the upgraded Giant Metrewave Radio Telescope (uGMRT) at low frequencies between 300 and 500 MHz. Apart from showing the

aforementioned consistency between results obtained with wide- and narrowband methods, Nobleson et al. (2022) also emphasize an increased precision of low-frequency DM measurements and prove wide-band timing methods to be beneficial even for small fractional bandwidths. Other examples of implementations of methods presented by Pennucci et al. (2014) can be found in Fonseca et al. (2021) and Sharma et al. (2022), where the analyses focus on detailed binary parameter estimation and study of new PTA-candidate pulsars, respectively.

Here we present wide-band timing of 35 ms pulsars observed with the UWL by the PPTA using PulsePortraiture (Pennucci et al. 2014, 2016). This is the first time such analysis is performed on observations gathered by a single ultra–wide-bandwidth receiver with instantaneous fractional bandwidth of approximately 6:1. It is also the first study of the new PPTA UWL data set in general (note, however, that UWL observations were used to estimate the DM for the timing analysis of the previous data release; Reardon et al. 2021). Continuous frequency coverage of an ultrawide band and utilization of PulsePortraiture allowed us to describe the evolution of pulse profiles and subsequently measure TOAs and DMs with raw uncertainties at least two times smaller than those obtained for the previous data set (Kerr et al. 2020, hereafter PPTA DR2).

The paper is organized as follows. In Section 2 we describe the UWL receiver, observation strategies, and the new data set. In Section 3 we present data preparation procedures and the principles of wide-band timing and noise analysis. Section 4 contains our results and their discussion, including profile evolution and timing models, noise analysis, and notes on a few individual pulsars. Summary and conclusions are presented in Section 5.

2. Observations

Observations analyzed in this paper were collected between 2018 November and 2022 March with the 64 m Parkes Radio Telescope (Murriyang) located in New South Wales, Australia. The starting date marks the transition from the previous observing systems to the UWL, which has been continuously carrying out all observations ever since. Full description and technical details of the new receiver and associated systems can be found in Hobbs et al. (2020), and below we introduce it only briefly.

Both the feed and low-noise amplifiers are cryogenically cooled and maintain low (22 K) temperature for the majority of the band. Preprocessed data consist of 26 critically sampled subbands, each 128 MHz wide, continuously covering the 704−4032 MHz frequency range. For timing purposes, we use data coherently de-dispersed and folded into 1024 phase bins by the DSPSR suite (van Straten & Bailes 2011) on the Medusa GPU cluster. Noteworthily, Medusa is the only processing system currently used, as opposed to seven employed in the previous data release PPTA DR2.

For flux calibration purposes we observe two bright sources (PKS B1934−638 and PKS B0407−658) approximately once per session. Additionally, each pulsar observation is preceded (and sometimes also followed) by a 2-minute injection of a noise diode signal.

The list of all 35 pulsars observed with the UWL for the PPTA project (P456) is presented in Table 1. Observations are carried out with a standard cadence of approximately 1−3 weeks. A total of 25 of the sources were included in the previous data release, while the remaining 10 were added to the array between 2018 and 2020 and are currently being reviewed as potential candidate pulsars for PTA.

---

[12] https://www3.mpifr-bonn.mpg.de/staff/pfreire/BEACON.html

Table 1
Summary of Timing Analysis for 35 Pulsars

Pulsar	Span (yr)	DM (cm^{-3} pc)	P (ms)	TOAs	Pars	rms (μs)	Med σ_{TOA} (μs)	Med σ_{DM} ($\times 10^{-4}$ cm^{-3} pc)	S/N	n_{eig}	Figure
J0030+0451*	3.1	4.33	4.87	34	5	0.784	0.732	4.423	427	1	7
J0125−2327*	3.1	9.60	3.68	105	13	0.529	0.129	0.974	5503	3	7
J0348+0432*	2.7	40.47	39.12	22	10	2.511	2.080	14.24	211	0	7
J0437−4715	3.3	2.64	5.76	222	13	0.195	0.005	0.043	18191	6	7
J0613−0200	3.4	38.78	3.06	76	13	0.269	0.158	0.807	1633	2	7
J0614−3329*	3.1	37.05	3.15	90	10	0.813	0.741	4.171	490	1	7
J0711−6830	3.3	18.41	5.49	157	7	0.435	0.550	3.211	3927	2	8
J0900−3144*	2.7	75.61	11.11	65	12	0.931	0.612	3.421	2376	2	8
J1017−7156	3.3	94.22	2.34	173	16	0.133	0.120	0.684	2090	2	8
J1022+1001	3.4	10.25	16.45	59	12	0.566	0.254	1.517	6189	3	8
J1024−0719	3.3	6.48	5.16	50	9	0.771	0.619	4.105	1516	2	8
J1045−4509	3.3	58.15	7.47	54	12	1.316	0.781	4.173	2408	2	8
J1125−6014	3.3	52.93	2.63	97	15	0.203	0.119	0.744	970	2	9
J1446−4701	3.3	55.83	2.19	73	13	0.665	0.425	2.741	431	0	9
J1545−4550	3.3	68.39	3.58	100	15	0.327	0.212	2.144	876	2	9
J1600−3053	3.3	52.33	3.60	53	16	0.263	0.113	0.832	2694	2	9
J1603−7202	3.3	38.04	14.84	105	12	0.706	0.361	2.129	6643	2	9
J1643−1224	3.3	62.41	4.62	42	14	1.25	0.286	1.459	2870	2	9
J1713+0747	2.3	15.92	4.57	43	13	0.241	0.048	0.384	9893	2	10
J1730−2304	3.3	9.62	8.12	39	6	1.244	0.287	1.677	3660	2	10
J1741+1351*	2.6	24.20	3.74	16	10	0.460	0.345	2.640	145	0	10
J1744−1134	3.3	3.14	4.07	88	8	0.327	0.080	0.524	8670	2	10
J1824−2452A	2.8	119.90	3.05	11	5	4.481	0.123	0.710	388	1	10
J1832−0836	2.7	28.20	2.72	21	8	0.246	0.227	2.107	290	1	10
J1857+0943	3.1	13.30	5.36	25	10	0.391	0.257	2.189	1366	2	11
J1902−5105*	2.7	36.25	17.40	31	7	2.884	0.329	1.910	121	0	11
J1909−3744	3.4	10.39	2.95	220	15	0.231	0.027	0.176	15208	1	11
J1933−6211*	3.1	11.50	3.54	84	12	0.752	0.764	4.842	1381	1	11
J1939+2134	2.7	71.01	1.56	12	5	0.856	0.010	0.050	2049	2	11
J2051−0827*	2.6	20.73	4.51	34	8	8.643	0.680	5.657	1462	2	11
J2124−3358	3.3	4.59	4.93	67	8	1.698	0.985	5.760	410	1	12
J2129−5721	3.3	31.85	3.73	109	12	0.679	0.509	3.512	1895	1	12
J2145−0750	3.3	9.00	16.05	51	13	0.823	0.186	1.179	7117	2	12
J2150−0326*	2.6	20.67	3.50	26	10	2.011	1.115	6.827	128	0	12
J2241−5236	3.3	11.41	2.19	151	13	0.283	0.070	0.465	8651	2	12

Note. Twenty-five of the listed pulsars are high-priority sources observed as part of the PPTA project, while the remaining 10 (marked with an asterisk) have been added to the array after the installation of UWL, between 2018 and 2020. The 10th column shows the S/N of the pulse portraits.

3. Methods

3.1. Wide-band Timing

We refer the reader to Pennucci et al. (2014) and Pennucci (2019) for a detailed explanation of the wide-band timing procedures; however, a brief summary is presented below.

We first make a smooth, noise-free, average (in time and frequency) profile from one highest signal-to-noise ratio (S/N) observation, which is then used iteratively to align several tens of epochs composing our initial frequency-resolved template. This step is similar for both narrow- and wide-band techniques; however, the standard phase shift between the profiles and the noise-free template is additionally a function of frequency, i.e., is described by a dispersion law:

$$\phi_n(\nu_n) = \phi_0 + \frac{K \cdot \mathrm{DM}}{P_S}(\nu_n^{-2} - \nu_{\phi_0}^{-2}), \qquad (2)$$

where ϕ_0 is the phase offset at reference frequency[13] ν_{ϕ_0}, $K = 4149.37759336 \, \mathrm{MHz}^2 \, \mathrm{cm}^3 \, \mathrm{pc}^{-1} \, \mathrm{s}$ is the dispersion

---
[13] The reference frequency is chosen such that there is zero covariance between DM and ϕ_0 (see Appendix in Pennucci et al. 2014).

constant, and P_S is the spin period of the pulsar. A collection of these aligned profiles (the portrait) is then decomposed into eigenvectors via principal component analysis (PCA), and the ones with the highest S/N (along with the mean profile) are used to model the frequency evolution of the profile. At the final step, a spline function is fitted to the projection of each mean subtracted portrait profile onto the significant eigenvectors. In short, we can reconstruct the profile shape at any desired frequency by summing up the product of n_{eig} spline functions $S_i(\nu)$ and significant eigenvectors $\hat{e}_i$ and adding it to the mean profile $\tilde{p}$:

$$T(\nu) = \sum_{i=1}^{n_{\mathrm{eig}}} S_i(\nu)\hat{e}_i + \tilde{p}. \qquad (3)$$

These procedures then allow for a simultaneous measurement of one TOA and DM per whole band (at a reference frequency ν_{ϕ_0}) for each observation by minimizing the statistic

$$\chi^2 = \sum_{n,k} \frac{|d_{nk} - a_n t_{nk} e^{-2\pi i k \phi_n}|^2}{\sigma_n^2}, \qquad (4)$$

where indices k and n run over Fourier frequencies and channels, respectively, d_{nk} is a one-dimensional (along phase axis) discrete Fourier transform (DFT) of the profile, and t_{nk} is the DFT of our template, a_n is the amplitude scaling factor, and σ_n^2 is the Fourier-domain noise level.

3.2. Data Preparation

In order to prepare data for our wide-band analysis, we first cleaned them from radio frequency interference (RFI), calibrated, and frequency-averaged down to 416 channels (each 8 MHz wide) by an automatic pipeline (also used in Kerr et al. 2020). Afterward, we prepared our portraits by aligning and averaging nearly all available UWL observations as explained in Section 3.1. The two exceptions here were the brightest or faintest sources. In the former case, $10-30$ observations were sufficient to produce high-S/N portraits and at the same time allowed for more accurate RFI excision. In case of the faintest sources in the data set, some of the observations were heavily corrupted by RFI or instrumental errors, and due to a much smaller number of observing epochs relative to brighter pulsars, they significantly affected the portrait and so were removed. We also note that each portrait was manually checked for RFI and channels with $S/N \sim 0$ before modeling procedures because (i) summing up the profiles may bring up previously missed contaminated channels and (ii) any spurious signal or impaired channels can significantly affect the model of profile evolution. Finally, once the templates were obtained, we derived spline models and subsequently measured one TOA and one DM per band for each observation as explained in Section 3.1. All of the above procedures were performed using an open-source code[14]— PulsePortraiture (Pennucci et al. 2014).

The last step before proceeding to timing analysis was to filter out all bad epochs in our data sets. For that purpose, we have defined four conditions that had to be met in order to include a particular observation in the further analysis:

1. Observation time: $t_{obs} > 300$ s. Nominal length of each observation is 1.1 hr. There is, however, a subset of shorter observations owing to technical limitations— changing weather conditions, finite length of observing session, RFI, etc. We include those partial observations in our analysis only if their length exceeds 300 s. Such a low threshold allows us to include more observations of the brightest pulsars, whereas short ones usually did not also fulfill the remaining conditions.

2. TOA S/N: $S > 25$. The quality of low-S/N observations results in poor estimation of measured TOAs and DMs (high uncertainties). Note, however, that the threshold applies to S/N of the wide-band TOAs, not observations, and is defined as $S \equiv \sqrt{\sum_n S_n^2}$, where $S_n \equiv a_n \sqrt{\sum_k |t_{nk}|^2} / \sigma_n$ (for a more detailed description see Appendix A in Alam et al. 2021b).

3. Goodness of fit: $\chi_{reduced}^2 < 1.25$. The χ^2 statistics is calculated for each observation, taking into account the model of profile evolution. Large values of this parameter can imply noncurated RFI or low-quality profiles.

4. Highest/lowest frequency ratio: $f_{ratio} > 1.1$. Observations filtered out based on this condition are either heavily contaminated by RFI or affected by serious instrumental

issues, where the signal throughout the majority of the band is lost. All observations that we included in our analysis had $f_{ratio} > 2.9$, which corresponds to the effective bandwidth of approximately 2600 MHz (most of the observations with $f_{ratio} \sim 2.9$ were cut below 1400 MHz owing to strong RFI). For full bandwidth $f_{ratio} = 5.7$.

This procedure allowed us to remove most of the bad epochs automatically, and only a small fraction of individual observations were later flagged manually owing to large residuals or DM/TOA uncertainties, which, as expected, occurred mainly for low-quality profiles. Each epoch that was commented out was additionally checked by eye to determine whether it could be curated and added back to the data set. This procedure was possible only because of a still relatively small number of observations; however, we acknowledge the need for more accurate RFI zapping algorithms for future analyses. In general, we used between 80% and 100% of available UWL observations for each pulsar.

Finally, we note that all of the pulsars in the data set were analyzed using total intensity profiles (Stokes I), apart from J0437−4715, for which we used the polarimetric invariant profile, as was also done in previous analyses (van Straten et al. 2001; Kerr et al. 2020). The invariant interval can be used to avoid additional red noise from polarization calibration errors and to reduce dependence of the observation on the parallactic angle (Hotan et al. 2006). It is given by Hotan et al. (2006):

$$S_{inv} = I^2 - Q^2 - U^2 - V^2, \qquad (5)$$

where I, Q, U, and V are Stokes parameters. It can be used in the case of the least polarized sources or when a large part of the emission is unpolarized, which is why we applied it only to J0437−4715. Our final data set consists of frequency-dependent profile templates (portraits), spline models of profile evolution, and a list of measured TOAs and DMs with their uncertainties for each pulsar.

3.3. Timing Solutions and Noise Analysis

As explained in Section 3.1, each wide-band measurement consists of one TOA and a corresponding DM at the time of the observation, along with their uncertainties. It is possible to obtain a wide-band TOA without fitting for the DM; however, that would still necessitate providing an external and precise measurement of the DM at the time of the observation in order to properly align the data with the template. Additionally, further analysis of the timing and noise models also requires using both measurements per observation, as opposed to subbanded TOAs, single wide-band TOA does not contain the full information of the dispersive delay within the observing band. In consideration of that, in our work we used two packages, i.e., Tempo (Nice et al. 2015) for pulsar timing and ENTERPRISE (Ellis et al. 2019) for noise modeling, where the new wide-band likelihood has already been implemented (alternatively, wide-band analysis can also be performed in PINT; Luo et al. 2021). The mathematical description of these implementations can be found in Appendix B of Alam et al. (2021b). Below, we present all details of obtaining our wide-band timing solutions and corresponding noise models, along with a general overview of the augmented likelihood.

---

[14] https://github.com/pennucci/PulsePortraiture/

We started with initial timing solutions obtained for the PPTA DR2 (Goncharov et al. 2021) applying the following changes. First, we removed all noise parameters, as they have to be derived again using the new wide-band likelihood. We have also updated the clock standard and solar system ephemeris to TT(BIPM2019) and DE438, respectively. Another change was applied to the choice of binary models. The majority of pulsars with binary companions from PPTA DR2 were fitted with the T2 model, which is available only in the Tempo2 package (Hobbs et al. 2006). Here, instead, for most pulsars we used the ELL1 model (adequate for low-eccentricity orbits; Lange et al. 2001), for one pulsar (J1643−1224) we used the DD model (to include measurement of eccentricity; Damour & Taylor 1992), for two pulsars (J0437−4715, J1713+0747) we used the DDK model (allowing for measurements of annual-orbital parallax; Kopeikin 1995, 1996), and four pulsars (J1017−7156, J1022+1001, J1545−4550, J1600−3053) were fitted with the ELL1H model (which includes modeling of Shapiro delay; Freire & Wex 2010).

The next element of our timing analysis is modeling of the DM variability. We used the DMX model, which assumes that the DM is constant within chosen time intervals (e.g., a fraction of a day or several days) and models the subsequent changes in a piecewise-constant manner. The choice of the DMX epoch length depends on various factors, e.g., observing strategy, desired precision, or expected ISM/solar wind variability. In this work we have applied DMX epochs between 1 and 60 days, depending on the number of measurements in order to avoid overfitting. Each DM from our wide-band measurements was then used as a prior on the DMX value in the corresponding epoch. In case there were more TOAs for a given epoch, the prior was calculated from a weighted average.

Finally, noise present in the timing residuals was modeled using Bayesian inference implemented within ENTERPRISE.

To account for the white noise, TOA uncertainties for each measurement σ_j^{ToA} were modified by two Gaussian-noise components:

$$\sigma_j^2 = (\mathrm{EFAC}\ \sigma_j^{\mathrm{TOA}})^2 + \mathrm{EQUAD}^2, \qquad (6)$$

where EFAC encapsulates unknown systematic errors associated with observing systems and analysis, and EQUAD added in quadrature characterizes any additional, system-independent white noise.

Within the wide-band likelihood, two new white-noise components have been introduced: DMEFAC and DMEQUAD, which are analogous to those described above but are applied to DM uncertainties. In addition to that, we also used a new DMJUMP parameter, which can be referred to the standard JUMP parameter (used to account for phase offsets of unmodeled profile evolution), but here it represents the offset between the mean wide-band DM and individual wide-band DM measurements. In other words, it accounts for the ambiguity of determining the absolute DM. Finally, a standard ECORR parameter can be omitted in the wide-band analysis, as it is describing the correlation between subbanded TOAs naturally not present here (noise sources contributing to ECORR are absorbed by EQUAD in the wide-band likelihood).

We set narrow Gaussian EFAC and DMEFAC priors on 1.00 ± 0.25. Priors for the other parameters are drawn from uniform distributions given by $\log_{10}(\mathrm{EQUAD}) \in [-8.5, -5.0]$,
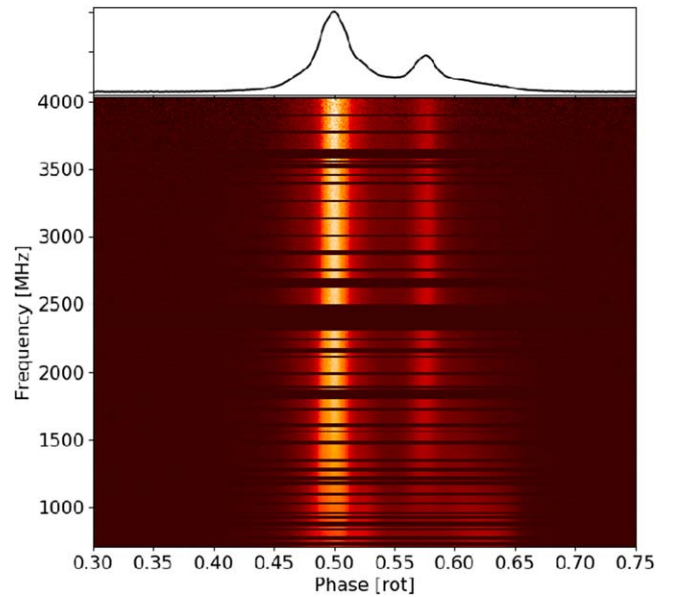

Figure 1. Data portrait of J0125−2327, with the mean profile shown in the top panel.

$\log_{10}(\mathrm{DMEQUAD}) \in [-7.0, 0.0]$, and $\log_{10}(\mathrm{DMJUMP}) \in [-0.01, 0.01]$.

4. Results and Discussion

Table 1 contains basic pulsar parameters and summarizes the results of our TOA/DM measurements and timing analysis. Apart from nominal DM, orbital period, median TOA/DM uncertainties, and rms of the timing residuals, we also listed the number of TOAs and fitted timing model parameters, the S/N of the average portraits, and the number of eigenprofiles as general characteristics of the profile evolution models. In Appendix A we show all the residual and DM variability plots (referenced in the last column of Table 1), and in Appendix B we present tables of our timing model parameters (Tables 2–8).

4.1. Average Portraits

As described in Section 3.1, an average portrait is composed of several tens of aligned and averaged observations. As an example, we show the portrait of J0125−2327 in Figure 1.

Each gap in frequency coverage corresponds to zero-weighted channels owing to strong RFI. The overall contamination of the whole band is relatively low, and the two most significant sources of spurious signal are mobile (<1000 MHz) and WiFi/Bluetooth (∼2400 MHz) transmissions.

Any residual intensity variations preserved despite time averaging of the portrait are eliminated by the normalization of each frequency channel with respect to the mean profile, and so the amplitude in Figure 1 is in arbitrary units. This procedure is meant to ensure that the model correctly describes the intrinsic profile shape changes irrespective of the effects of spectral index or ISM variability (specifically the diffractive scintillation).

4.2. Profile Evolution Models

Profile evolution with frequency is encoded in the spline curve model, and the number of significant eigenvectors (eigenprofiles) can be treated as a proxy for the level of profile
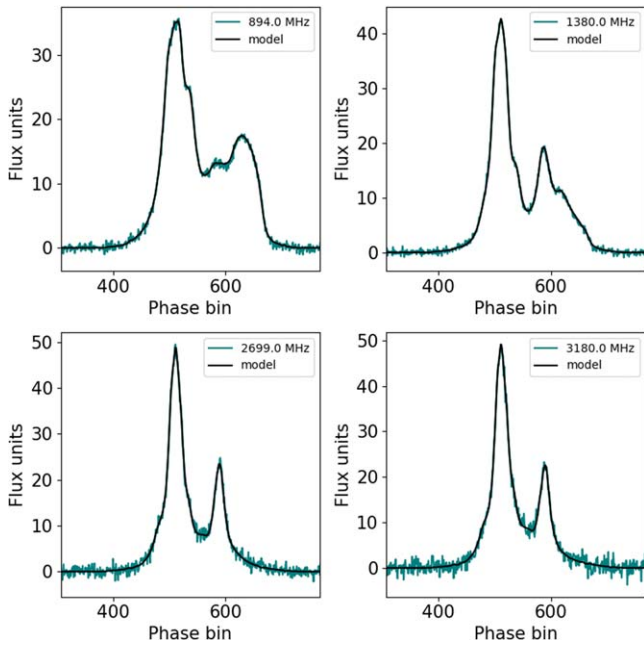
Figure 2. Pulse profiles observed (teal) and reconstructed by the spline model (black) at four frequencies throughout the UWL band for J0125−2327 (upper left to lower right: 894, 1380, 2699, and 3180 MHz).

Figure 3. Mean profile and three eigenprofiles for J0125−2327. Units at the y-axis are arbitrary.

evolution complexity. Noteworthily, the latter depends not only on the intrinsic profile shape changes but also on any distortions of the signal (e.g., due to ISM or RFI) and observing system/analysis failures.

When there are no eigenprofiles detected, all measurements are referred to the mean profile. In such a case, either there is none/little profile evolution, or the S/N for a given pulsar is too low. The first eigenprofile corresponds to a gradient of the mean profile changes (provided that it is the only eigenprofile detected), while the second and third may encompass a more extreme profile evolution, possible ISM effects such as unmodeled scattering, or issues related to data reduction and analysis. These could be, e.g., misalignment of the profiles composing the average portrait and inaccuracies in polarization calibration. More than three eigenprofiles can be detected for very high S/N pulsars, but usually they arise from systematic errors or unmitigated RFI.

The number of eigenprofiles for each pulsar in our data set is listed in Table 1. The majority of pulsars required two eigenprofiles (19 out of 35), one was detected for eight pulsars, and none were detected in the case of five sources. The remaining three pulsars were described by three (J0125−2327, J1022+1001) and six eigenprofiles (J0437−4715). There is an evident relation between the complexity of the spline model and the S/N of the average portrait, indicating that the quality of observations is one of the leading factors affecting the precision of pulse shape modeling. We discuss this further in Section 4.3.

Below, as an example, we present the profile evolution model for J0125−2327. This is a new pulsar to the PPTA discovered in the Green Bank Northern Celestial Cap Pulsar Survey (Stovall et al. 2014), characterized by a profile with two leading components exhibiting strong evolution with frequency. Figure 2 shows the observed profile shapes at four frequencies throughout the UWL band extracted from the
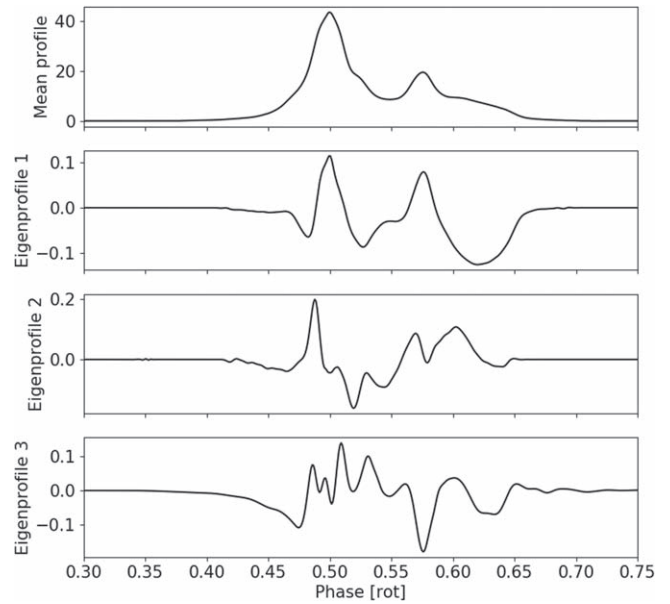
average portrait (teal) and modeled pulse profiles (black). Despite obvious complexity of the pulse shape and its evolution, the model is closely tracing all visible details with high accuracy.

J0125−2327 is one of only three pulsars for which we detected three significant eigenprofiles (shown in Figure 3). Each eigenprofile is smooth and well resolved with a high S/N. Additionally, coordinate curves composing the spline model shown in Figure 4 are clear and do not exhibit any signs of RFI contamination. In fact, the presented model can be considered as a flagship example given the complexity of the pulse shape and the level of detail captured.

In the case of the majority of our pulsars that are described by two high-S/N eigenprofiles, their spline models do not indicate any substantial issues and fit observed profiles at various frequencies with a comparable level of accuracy to that shown above. Five out of 35 pulsars with no significant eigenvectors have portrait S/N < 430, usually with low flux measured above 2500 MHz. Similarly, subtle profile shape characteristics and its changes can be lost for models with only one eigenprofile, especially in the upper part of the band, where the flux of most pulsars is usually lower. Two extreme examples of such sources are J0030+0451 and J2129−5721, both with large spectral indices, $\alpha_{J0030} = -2.4$ and $\alpha_{J2129} = -3.9$, respectively (Spiewak et al. 2022). In order to capture any profile evolution and more accurately predict the pulse shapes at lower frequencies, we decided to remove the upper part of the band above 3000–3500 MHz. This resulted in a detection of a previously not present eigenprofile for J2129−5721 and a much better fit to the observed profile shapes in the case of both pulsars.

Finally, we would like to stress that the fact that all pulsars we studied required only zero to three eigenprofiles indicates excellent quality of UWL observations maintained throughout the whole band (free of substantial instrumental, calibration, or profile alignment errors). In addition to that, our study demonstrates a notable efficiency of PulsePortraiture, where
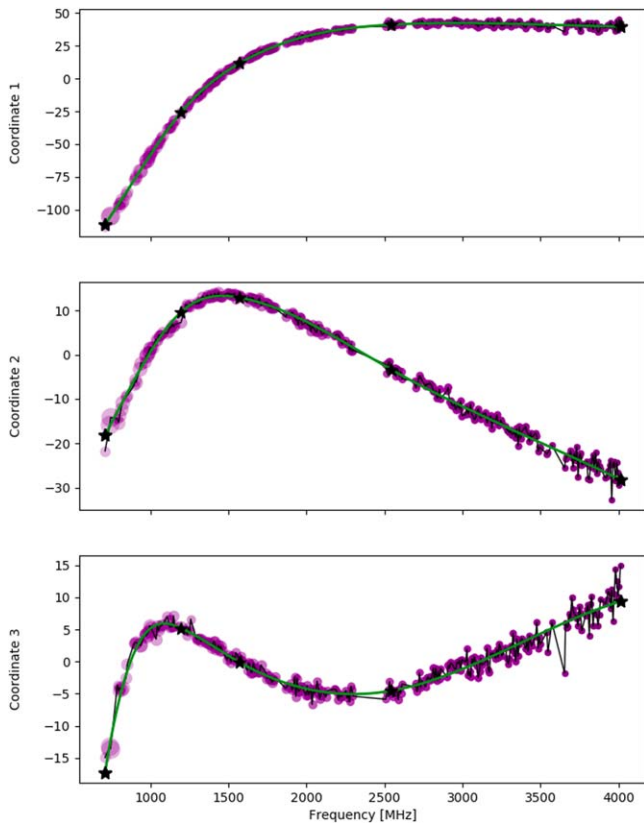
Figure 4. Spline model of profile shape evolution with frequency for J0125–2327. Purple points are mean subtracted profiles composing the average portrait projected onto the eigenprofiles. Color scale and size of the points correspond to frequency and S/N of the profile, respectively. The green line represents the spline model of profile evolution.

even complex pulse shape changes can be captured and described by a reasonably simple model.

4.3. Subbanded TOAs

Although wide-band timing methods offer a number of improvements, such as simplification of timing models and lowering data volumes, a parallel analysis of subbanded TOAs may help reveal frequency-dependent effects related to physical phenomena, such as DM variations, or technical issues. At the same time, wide-band profile evolution modeling is also sensitive to instrumental problems (e.g., resulting in spurious eigenprofiles) and was shown to improve timing of scintillating and weak pulsars (Alam et al. 2021b). Moreover, comparison of noise models from narrow- and wide-band data sets can help discriminate various sources of noise because of a different set of parameters. Therefore, synergy between the two approaches would be highly beneficial for high-precision pulsar timing, allowing for better characterizations of individual pulsars, ISM, and their models.

Following the above arguments, we divided all UWL observations into eight subbands and calculated wide-band TOAs separately in each band, using the model derived for the whole band. The first six bands have an equal width of 208 MHz and cover a frequency range from 704 to 1952 MHz, while bands 7 and 8 are broader (416 and 1664 MHz, respectively), providing a more even distribution of S/N.

In Figure 5 we present subbanded residuals as a function of time and frequency (top and bottom panels, respectively) and DM measurements for pulsar J0125−2327 as an example. This is one of the best-timed sources in our sample, with $\sigma_{\mathrm{TOA}} = 129$ ns, a portrait with high S/N = 5503 and a detailed model containing three well-defined eigenprofiles presented in Section 4.2. Nevertheless, the bottom panel of Figure 5 shows an evident frequency drift of the residuals with an amplitude of approximately 3.79 μs. After a thorough inspection, we found such drift in all of our pulsars, but with varying significance. The median amplitude of the drift is about 1.65 μs, and in most cases it lies below the phase bin resolution.

This leads to the first hypothesis: if pulse shape changes occur at such small scales, then the spline models may not be able to capture their frequency evolution in full detail, resulting in frequency dependence of the residuals. However, we find that scenario unlikely, as power spectra of the average portraits show an expected exponential drop of the signal with harmonic number, while any unresolved features would remain above the white noise at all harmonics.

More importantly, phase resolution can be a limiting factor in the process of profile alignment for the average portraits. As noted in Pennucci (2019), intrinsic profile evolution is entangled with the absolute DM or its variations, and the alignment of the portraits may be accurate up to one phase bin level. Furthermore, due to the dispersive law, any inaccuracies in the DM measurements will induce profile smearing on timescales increasing with bandwidth; thus, the effect will be more prominent for ultra–wide-band receivers, such as the UWL. The rotational period of J0125–2327 is 3.68 ms, which means that the amplitude of the frequency drift seen in Figure 5 is equal to approximately one phase bin, further supporting this scenario. The corresponding δDM that would induce this level of drift across the UWL band is $\sim 5 \times 10^{-4}\,\mathrm{cm}^{-3}$ pc, which is comparable to the median DM uncertainty of $\sim 1 \times 10^{-4}\,\mathrm{cm}^{-3}$ pc.

Another possibility is that these drifts are induced or enhanced by timing and noise modeling systematics or during the decomposition of the average portraits with PCA, which can be supported by the form of their frequency dependence. Of course, all of the above hypotheses do not have to be mutually exclusive, and the observed frequency drift may very well be a function of multiple factors.

Pulsars, where the drift is larger than the bin resolution, have either zero (J1446−4701) or one eigenprofile (J2124−3358 and J2129−5721), have a broad profile possibly affected by scattering (J1045−4509), and have a weak uppermost part of the band that was cut out during modeling (J2129−5721). In these cases we expect some of the information on the profile evolution to be missing or obscured, and therefore a few possible improvements would require observations with higher S/N and detailed modeling of the ISM effects.

This work is the first to report and delineate the unmodeled frequency dependence in the timing residuals from wide-band timing, although PulsePortraiture and wide-band techniques have already been used for multiple and diverse studies as was mentioned in Section 1. The phenomenon is naturally present in narrowband analyses that use frequency-averaged templates and is usually corrected by applying additional FD parameters to the timing model in order to account for profile evolution with frequency. The main goal of the wide-band technique is to capture and model these frequency-dependent effects, and thus
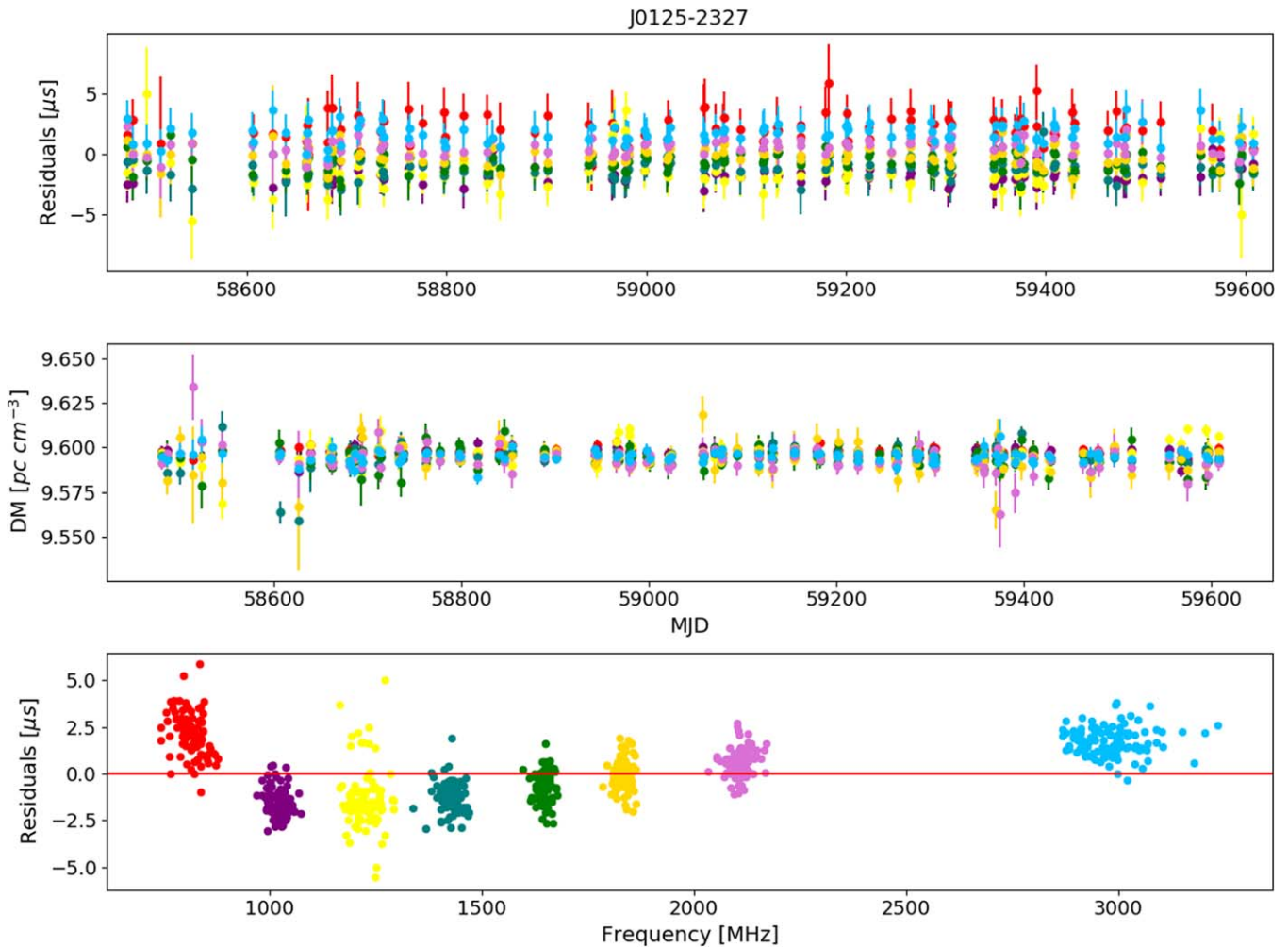
Figure 5. Subbanded residuals and DM measurements for J0125−2327. The bottom panel shows residuals as a function of frequency. Each color corresponds to one of the frequency bands.

detection of the drift in our wide-band data is unsettling. We note, however, that a similar trend has recently been detected also in other data sets including wide-band analysis from NANOGrav (via private communication). Additionally, timing models from the latest MPTA release included FD parameters despite using frequency-evolving templates (Miles et al. 2023).

The fact that the drift was observed only now may have multiple reasons. Frequency-dependent phenomena will be less pronounced or even absolutely undetectable for narrow-bandwidth observations, and wide-band timing methods have, in fact, never been used on data with more than 2 GHz instantaneous frequency coverage and to such extent (nearly all new timing analyses now include wide-band methodology). For instance, wide-band analysis presented in NG12.5 did not report the need for FD parameters because the TOAs were effectively calculated only for two subbands (as opposed to eight subbands shown in Figure 5), which obscured any such detectable drifts. Similarly, Tarafdar et al. (2022) also presented both narrow- and wide-band timing of 14 pulsars as the first data release from the InPTA and explicitly showed no need for additional corrections for frequency-dependent effects. However, InPTA analysis was also performed on only two subbands and produced narrowband, frequency-resolved templates by iteratively fitting for DM to the multiband observations. Noteworthily, Tarafdar et al. (2022) pointed out that

differences in denoising the templates lead to a discrepancy in DM estimates obtained by narrow- and wide-band techniques, which might be worth further investigation.

Interestingly, parallel narrow- and wide-band analyses presented in, e.g., NG12.5 and Nobleson et al. (2022) yielded remarkable agreement between the results from the two methods. This indicates that frequency-evolving templates and wide-band measurements provide timing precision at least as good as standard procedures despite the observed frequency drift; however, its actual significance will be a matter of debate. This argumentation also applies to this work, as TOA/DM uncertainties and rms of the residuals we obtained reach low, submicrosecond precision, which is an improvement when compared to PPTA DR2. A complete and fully restrictive comparison will be possible after obtaining narrow- and wide-band results for the next PPTA data release, which is already in the process of preparation.

Nevertheless, observed frequency dependence of the residuals is a noteworthy complication because wide-band timing aims to model all frequency-dependent effects in its extraction of a single TOA per observation, thus rendering ad hoc frequency-dependent modeling of the timing residuals obsolete. The solution to this problem is beyond the scope of this work but is under investigation in several groups.

4.4. Timing Models

The nominal set of fitted parameters in our timing models included spin period P, spin down rate P1, and five astrometric parameters: right ascension (R.A.) and declination (decl.), proper motion in both directions PMRA and PMDEC, and parallax PX. Binary pulsars were additionally fitted for orbital period PB, projected semimajor axis A1, epoch of ascending node TASC, and first and second Laplace parameters (EPS1 and EPS2, respectively). For a few pulsars, proper motions and parallax were poorly constrained, so we excluded them from the fitting. In particular, this is the case of pulsars close to the ecliptic such as J1022+1001 and J1730−2304. Additionally, the first time derivative of orbital period PBDOT, rate of change of periastron OMDOT, and projected semimajor axis XDOT also could not be measured for most pulsars and were excluded (except from models for J0437−4715, J1017−7156, and J2145−0750). For all four pulsars with the ELL1H binary model we find both orthometric Shapiro delay parameters H3 and H4. Finally, in the case of two pulsars with a DDK binary model (J0437−3715 and J1713+0747), instead of fitting for the aforementioned binary parameters, we used epoch and longitude of periastrion (T0 and OM, respectively) and eccentricity of the orbit (E). Tables containing the timing results are presented in Appendix B. Timing model parameters we obtained are consistent with those presented in PPTA DR2 within error limits. The most significant discrepancies were measured for PMRA, PMDEC, and PX parameters, which is expected because of the much shorter length of our data set (e.g., PX for J2145−0750 obtained by us and that in PPTA DR2 are 3.4(7) and 1.40(8), respectively).

4.5. Noise Analysis, Timing Residuals, and DM Variations

For the majority of our pulsars EFAC and DMEFAC parameters have values between 1.0 and 1.3, which indicates that the TOA and DM measurements are free of substantial systematic errors (note, however, that this is also a function of narrow prior distributions).

There are two pulsars with excess white noise characterized by a slightly increased DMEFAC (J2124−3358 and J2241 −5236) up to 1.58 and 1.41, respectively. The absolute value of the DMJUMP parameter in most cases is less than 0.0007 cm^{-3} pc indicating a proper alignment of profiles composing the average portrait and a consistent fit for DM from modeling and noise analysis. There are, however, two pulsars (J1824 −2452A and J2051−0827) where DMJUMP goes up to 0.009, and there might be several reasons for that, including significant scattering, large DM variations, or simply the fact that they have much less data than other pulsars in the data set. Additionally, J2051−0827 is a black widow (eclipsing binary), and together with aforementioned ISM effects, this can impede obtaining a correct profile alignment.

Our initial noise models for most pulsars are dominated by large EQUAD values of the order of a few hundred nanoseconds. This is due to the fact that EQUADs absorb all of the unmodeled sources of noise, including all kinds of red noise but also jitter and issues with modeling the DM variability (usually covered by the ECORR parameter, which is omitted in wide-band methodology). We have obtained submicrosecond rms in 26 pulsars, out of which 20 belong to the main PPTA array. Nearly all pulsars (94%) have median TOA uncertainties lower than 1 μs, except for two low-priority

sources that have been observed by the PPTA only recently (J0348+0432 and J2150−0326). In the case of DM uncertainties, our measurements are in the range of $(0.043–14.24) \times 10^{-4}$ cm^{-3} pc. We have obtained DM precision of 10^{-5} cm^{-3} pc for 10 pulsars and down to 10^{-6} cm^{-3} pc in the case of two (J0437−4715 and J1939+2134). This is the level of precision achieved by Nobleson et al. (2022) for corresponding pulsars despite the fact that their observations covered the 200–500 MHz band, where DM measurements can be measured with higher precision because of the larger delays and stronger signal in the low-frequency regime.

Finally, we would also like to note an observed dependence of the DM on usable bandwidth (cleaned of all spurious channels). For instance, there is a subset of observations where $f_{ratio} < 3$ because the lower part of the band (below 1400 MHz) was cut out by automatic pipelines owing to strong RFI. Usually, this resulted in lower or higher estimated DMs when compared to the ones obtained for the whole band even by ~ 0.005 cm^{-3} pc (see, e.g., residuals for J0125−2327 in Appendix A), which is at least one order of magnitude larger than the typical DM uncertainty obtained in the data set. This effect might be correlated with the observed frequency drift of the residuals reported in Section 4.3 or to the frequency-dependent DM (explained further in Section 4.7.2) and will be investigated together in future work.

4.6. Pulsars Not Included in the Main PPTA Array

Apart from the top-priority pulsars observed for nearly two decades, PPTA has also been monitoring 10 new and/or lower-priority sources since the start of UWL operation. Their timing potential is currently being investigated, and this work may serve as an additional point for their evaluation (R. Mandow et al., in preparation).

Most of these pulsars (6 out of 10) have low S/N (<500), which makes modeling of their profile evolution difficult; however, their TOA uncertainties reach precise timing requirements with values between ~350 and 700 ns (apart from J0348+0432 and J2150−0326 already mentioned in the previous section). The remaining four sources have high S/N and low TOA uncertainties in the range of 129–764 ns. Their models are characterized by good resolution and up to three eigenprofiles, including a fine example of J0125−2327 discussed in detail in Sections 4.1 and 4.3. Pulsar J0900 −3144 is already a part of EPTA with a timing baseline of approximately 7 yr and TOA precision of 4.27 μs (Desvignes et al. 2016), while our work gives $\sigma_{TOA} = 0.612$ μs, which indicates that this is a source worth further monitoring. J1933 −6211 has a profile shape with the multipeak leading component strongly evolving with frequency; however, we detected only one eigenprofile for it. Further monitoring and collecting more observations would be highly beneficial for a better characterization of this pulsar, especially given that it is a typical binary pulsar with a white dwarf companion (Graikou et al. 2017), which makes it a potentially valuable addition to the PPTA project. J2051−0827 is relatively bright (S/ N = 1462); however, it is one of the most difficult sources in our sample to describe. Its pulse shape consists of one peak component strongly affected by scattering; additionally, it is an eclipsing binary, so modeling its profile evolution and noise analysis are particularly challenging. J0348+0432 and J2150 −0326 are the worst two pulsars in our sample in terms of median TOA uncertainties, so directly they might not be of

much value to the PPTA (although further observations and individual analysis may improve their solutions). Nevertheless, monitoring such sources can also lead to a better understanding of pulsars emission or ISM effects, which in turn may help in constructing better timing and noise models in general (Kerr et al. 2020).

Finally, we also report the measurements of the binary orbital periods for two pulsars that were not previously published: J0125−2327 and J2051−0827 (Tables 2 and 7 in Appendix B).

4.7. Notes on Individuals Pulsars

4.7.1. J1022+1001

J1022+1001 is an interesting source because of a long-standing controversy regarding its pulse shape instability over timescales ranging from several to several tens of minutes (see Padmanabh et al. 2021 and references therein). There have been various attempts to explain this peculiar behavior, which include suggested polarization calibration errors (van Straten 2013), strong scintillation coupled with intrinsic profile evolution (Shao & You 2016), or effects directly related to the pulsar magnetosphere (Ramachandran & Kramer 2003). Unfortunately, there is still no consensus, as these results are often contradicting. In our wide-band model for this pulsar, a complex shape evolution is evident, as the two-peak pulse components change their relative height. Notwithstanding, the reconstructed profiles trace the shape evolution with a good precision (similarly to the model of J0125−2327 shown in Figure 2).

The spline model for J1022+1001 profile evolution required three eigenprofiles. They can correspond either to subtle corrections to the intrinsic profile shape changes or to the absorbed ISM/instrumental effects as was mentioned earlier in Section 4.2. It might be tantalizing to discern temporal pulse shape variability in the second and/or third eigenprofile, although spline models are supposed to trace only stationary profile changes with frequency. The initial noise model returns a very large EQUAD of 1.4 μs, which is significantly exceeding recently estimated jitter of $\sim$120 ns for 1 hr integration (Parthasarathy et al. 2021), and this might indeed reflect the scatter induced by pulse instability in time (and other noise sources as explained in Section 4.5).

4.7.2. J2241−5236

Frequency-dependent DM (Cordes et al. 2016) is thought to be detectable mostly for bright, high-DM pulsars with little to no profile evolution, which would make J2241−5236 a nearly perfect target. If a true nature of phase offsets deviates from ν^{-2} given by the dispersion law (Equation (2)), the DM measured at different parts of the band will vary. In fact, detection of this phenomenon for J2241−5236 was recently reported by Kaur et al. (2022) based on 3 days of observations obtained by uGMRT, Murchison Widefield Array (MWA), and Parkes UWL in 2019 November. The reported DM changes scale as δDM $\sim \nu^{2.5\pm0.1}$, indicating that DM measured at lower frequencies is notably higher than the one measured in the upper part of the band.

In our wide-band analysis, we have initially obtained a similar trend when studying 20-minute integrations and a data portrait consisting of approximately 10 highest-S/N observations. The number of detected eigenprofiles strongly depended
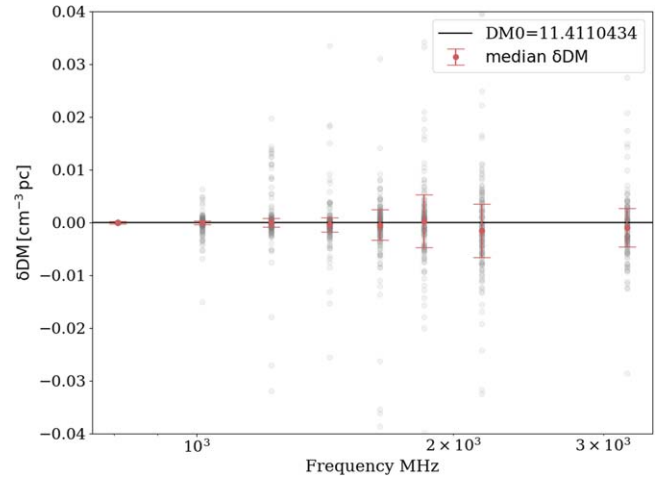

Figure 6. Subbanded DM measurements as a function of frequency for J2241−5236. Gray circles represent each individual measurement, while red points show median values and their uncertainties for each subband. The y-axis on the plot was narrowed down to δDM in the range of (−0.1, 0.1) cm^{-3} pc for a better visibility, omitting a few outlying measurements; however, they were included in the calculation of the median value. Nominal DM is shown in the legend of the plot, and it corresponds to the black line centered at δDM = 0.

on the number of used channels (it was either zero or one) despite the overall S/N exceeding 3500. In the final analysis we have used full 1 hr integrations and all available UWL observations, which resulted in doubling the S/N of average portraits for most pulsars. Our new model for J2241−5236 has two well-resolved eigenprofiles, and the subbanded residuals show a small frequency drift of 0.67 μs relative to a bin width of 2.14 μs.

In Figure 6 we show subbanded DM measurements as a function of frequency. All of our DM measurements now have δDM $\sim$ 0 with respect to the nominal DM, and so any chromatic trend of the DM detected previously was reduced significantly.

These results indicate that detection of frequency-dependent ISM phenomena may be more difficult than previously expected. Even best candidate pulsars with sharp integrated profile shapes and high stability may exhibit nonnegligible profile evolution at small submicrosecond scales, which is challenging both to detect and to model. Additionally, we would like to emphasize again that the measured results will be a function of the somewhat arbitrarily determined profile evolution model and disentangling this from actual ISM or other frequency-dependent effects is a nontrivial problem (Hassall et al. 2012).

5. Summary and Conclusions

We have presented wide-band timing analysis of the new UWL observations collected under the PPTA project between 2018 November and 2022 March. The main output of our work is a presentation of precise models of profile shape evolution with frequency for 35 pulsars and wide-band timing measurements (simultaneously estimated TOAs and DMs). We have also performed an initial noise analysis extended with wide-band likelihood including white-noise components. Results presented here are the very first demonstration of using methods presented in Pennucci et al. (2014) on observations with instantaneous bandwidth larger than 2 GHz (fractional

bandwidth of UWL is 1.41), which is soon to become a standard in high-precision pulsar timing.

Precision of our TOA and DM measurements is in the range of 0.005–2.08 μs and (0.043–14.24) $\times$ 10^{-4} cm^{-3} pc, respectively. Comparison of raw TOAs from our work and the previous data release PPTA DR2 yields an increase of the precision by a factor of two; however, due to utilization of different receivers, back ends, and analysis methods, this gives only a rough yet promising estimate. A proper comparative analysis will be possible after finalization of two parallel releases (narrow- and wide-band) comprising all available PPTA data extending back to 2004.

In the case of two pulsars, J0030+0451 and J2129−5721, very low S/N above 3000 or 3500 MHz affected the accuracy of the modeled profile evolution. We decided to exclude the uppermost frequencies from our analysis, which improved both models; however, wide-band timing procedures should ultimately be able to resolve such issues in a less brute-force manner. For instance, this could be achieved by adjusting the normalization algorithm so that it does not artificially elevate or overestimate information from low-S/N channels.

We have detected a frequency drift of the subbanded residuals obtained with wide-band methodology with an average amplitude of ∼1 μs, which is below the phase bin resolution of our observations. This might indicate profile alignment issues; however, we cannot yet rule out other possible explanations, including timing/noise model systematics, nuances of PCA procedures, and the effect of non- or poorly modeled ISM effects, such as scattering. The frequency dependence of the residuals will be investigated further in detail, and the results will be presented elsewhere.

Wide-band models presented here will be used for timing analysis of the next full data release (DR3) from PPTA, which is now under development. The nominal DR3 data set, despite using frequency-evolving templates, will produce subbanded TOAs of UWL observations in order to combine them with the previous releases in a consistent way. However, we also do intend to produce a wide-band DR3 in parallel, where we will reproduce 14 yr long data sets with methods presented here and combine it with UWL observations.

Appendix A
Timing Residuals and DM Measurements

In Figures 7–12 we present plots with timing residuals (top panels) and DM variability (bottom panels). For each pulsar, TOA error bars are corrected by the obtained white-noise components, namely EFAC and EQUAD, while DM measurements include DMEFAC and DMJUMP. Red and black points in DM plots show the wide-band measurements and DMX model, respectively. If DMX model points are missing in any pulsar plot, it means that there is only one DMX bin encompassing the whole timing baseline. This is the case for the least frequently observed pulsars.
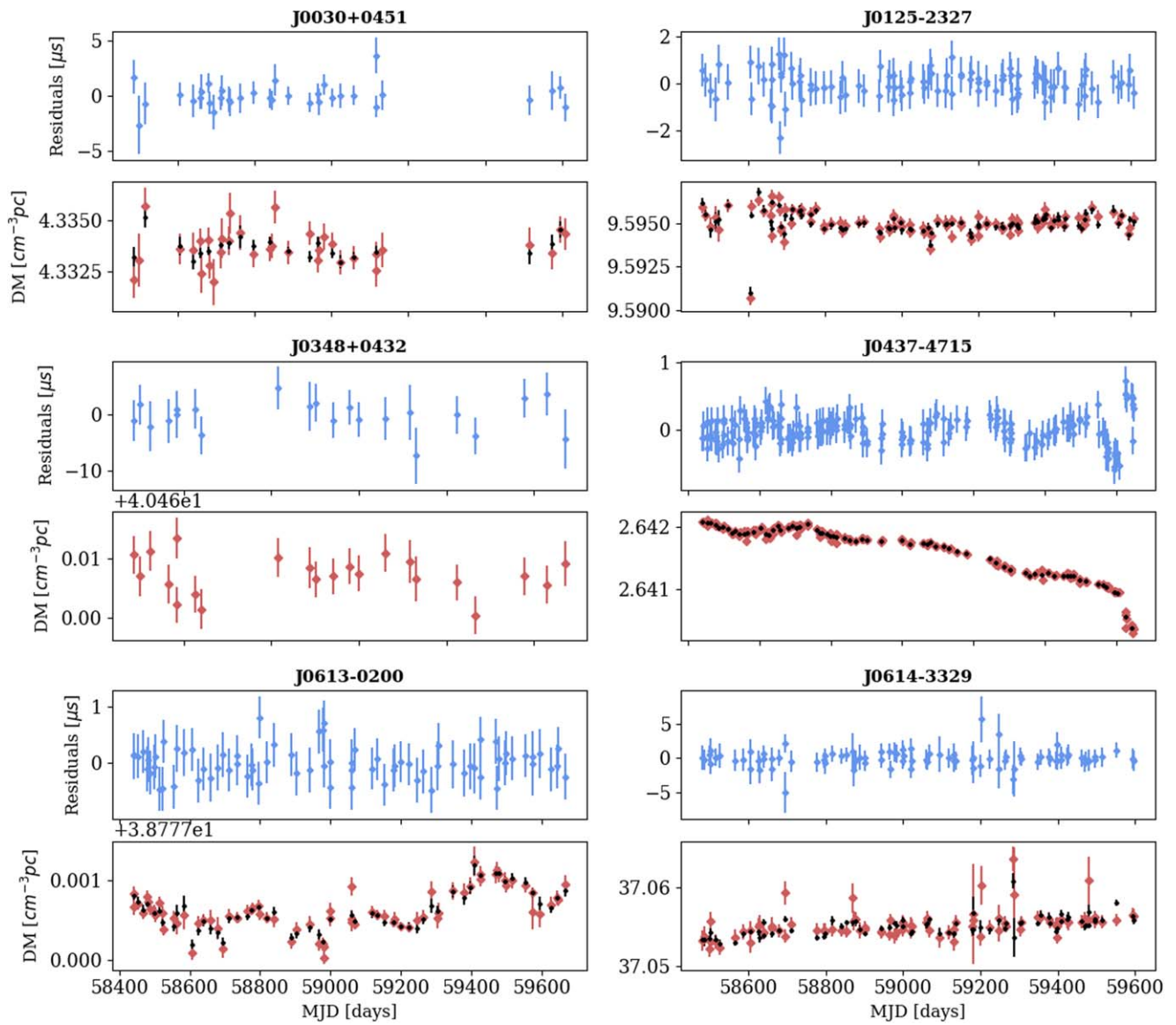
Curyło et al.

Figure 7. Timing residuals and DM variations for J0030+0451, J0125−2327, J0348+0432, J0437−4715, J0613−0200, and J0614−3329.
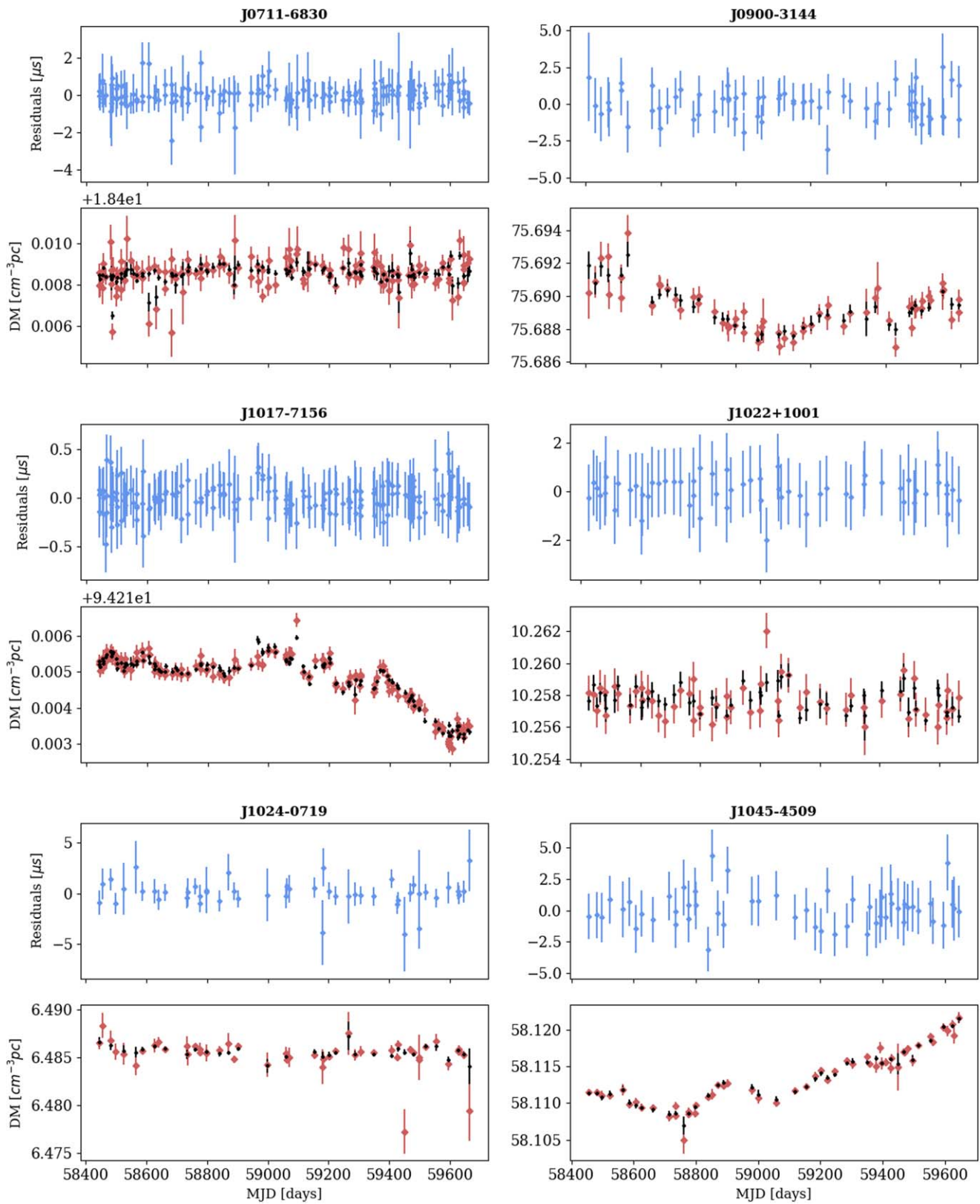
Figure 8. Timing residuals and DM variations for J0711−6830, J0900−3144, J1017−7156, J1022+1001, J1024−0719, and J1045−4509.
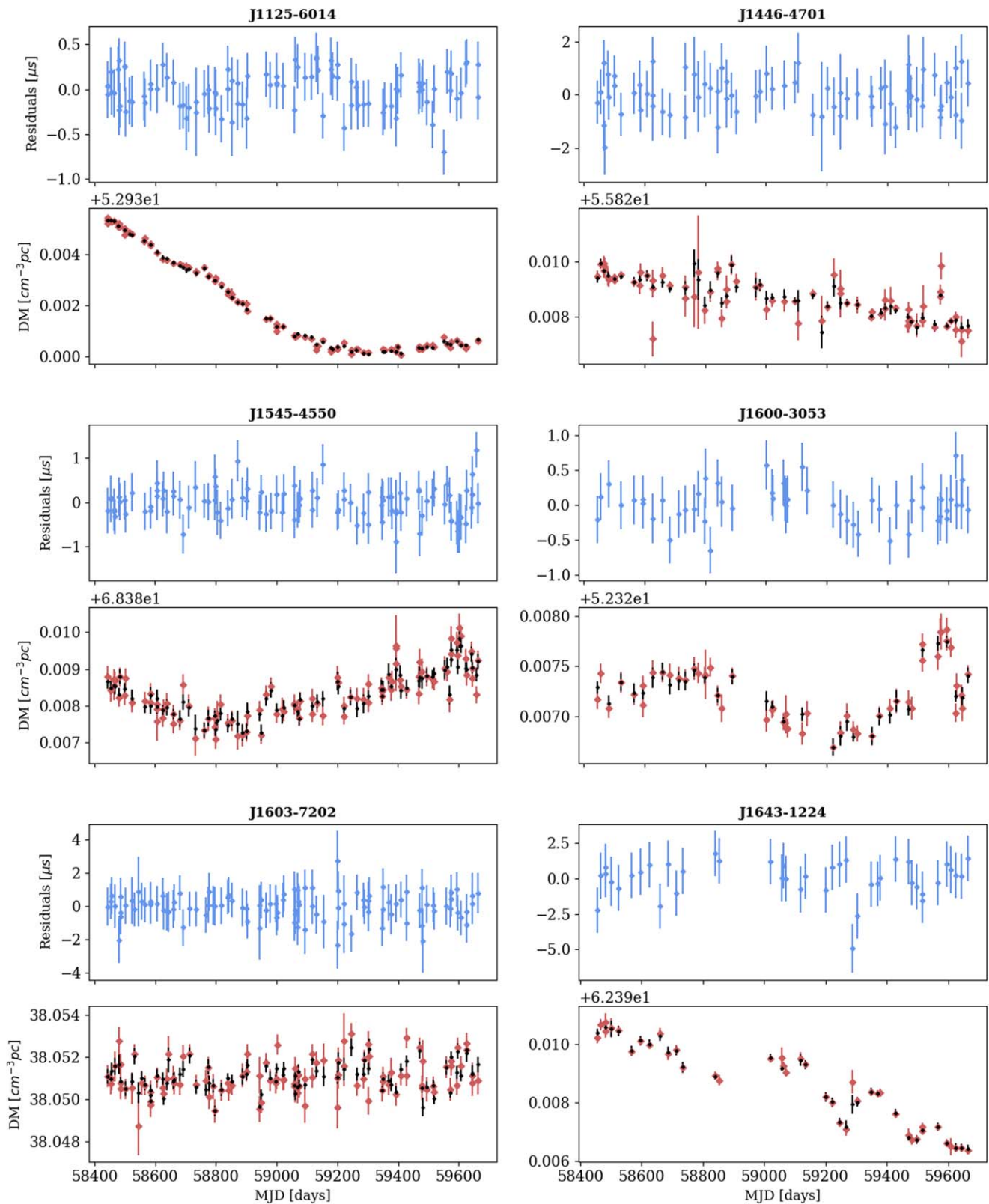
Figure 9. Timing residuals and DM variations for J1125−6014, J1446−4701, J1545−4550, J1600−3053, J1603−7202, and J1643−1224.
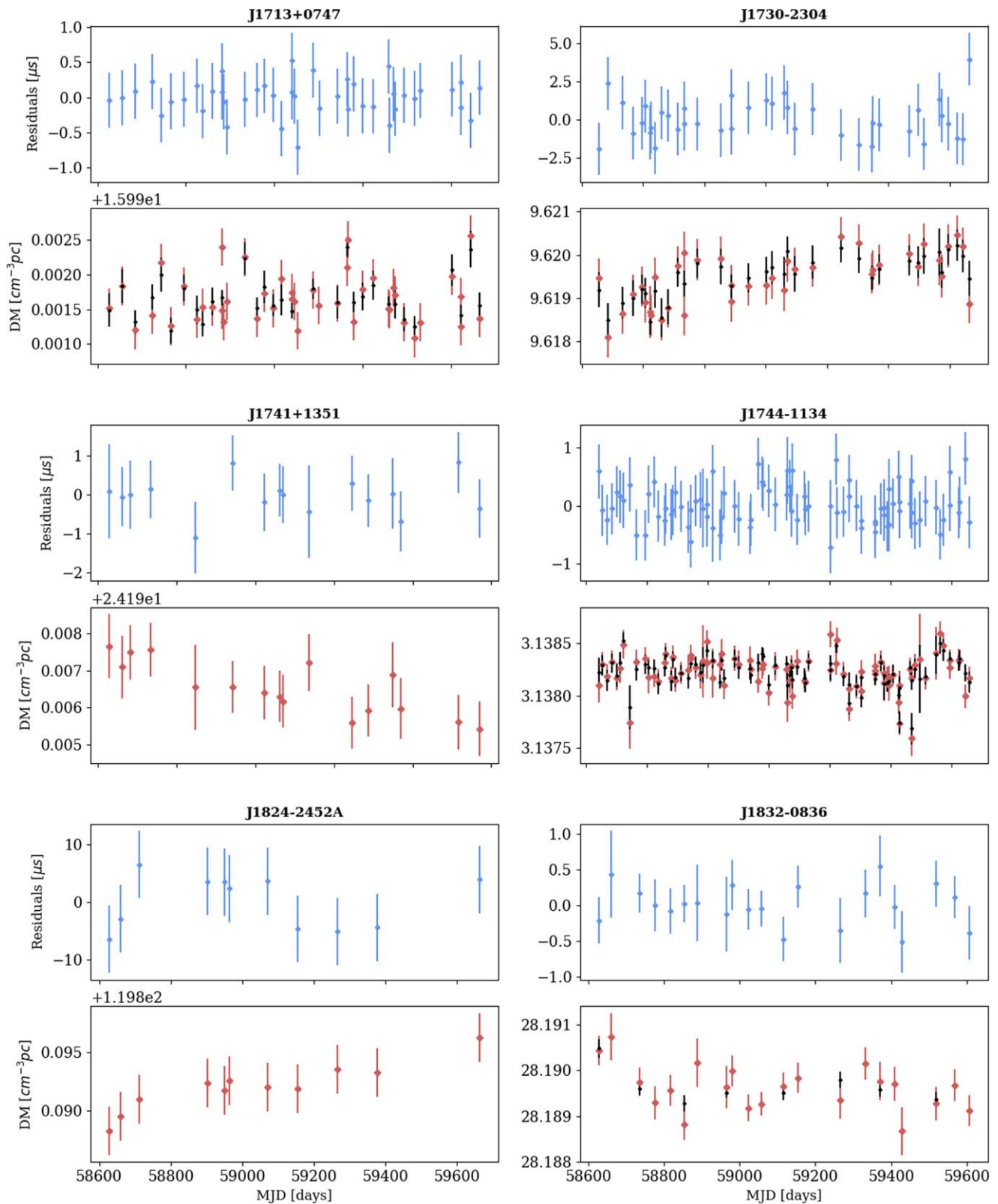
Figure 10. Timing residuals and DM variations for J1713+0747, J1730−2304, J1741+1351, J1744−1134, J1824−2452A, and J1832−0836.
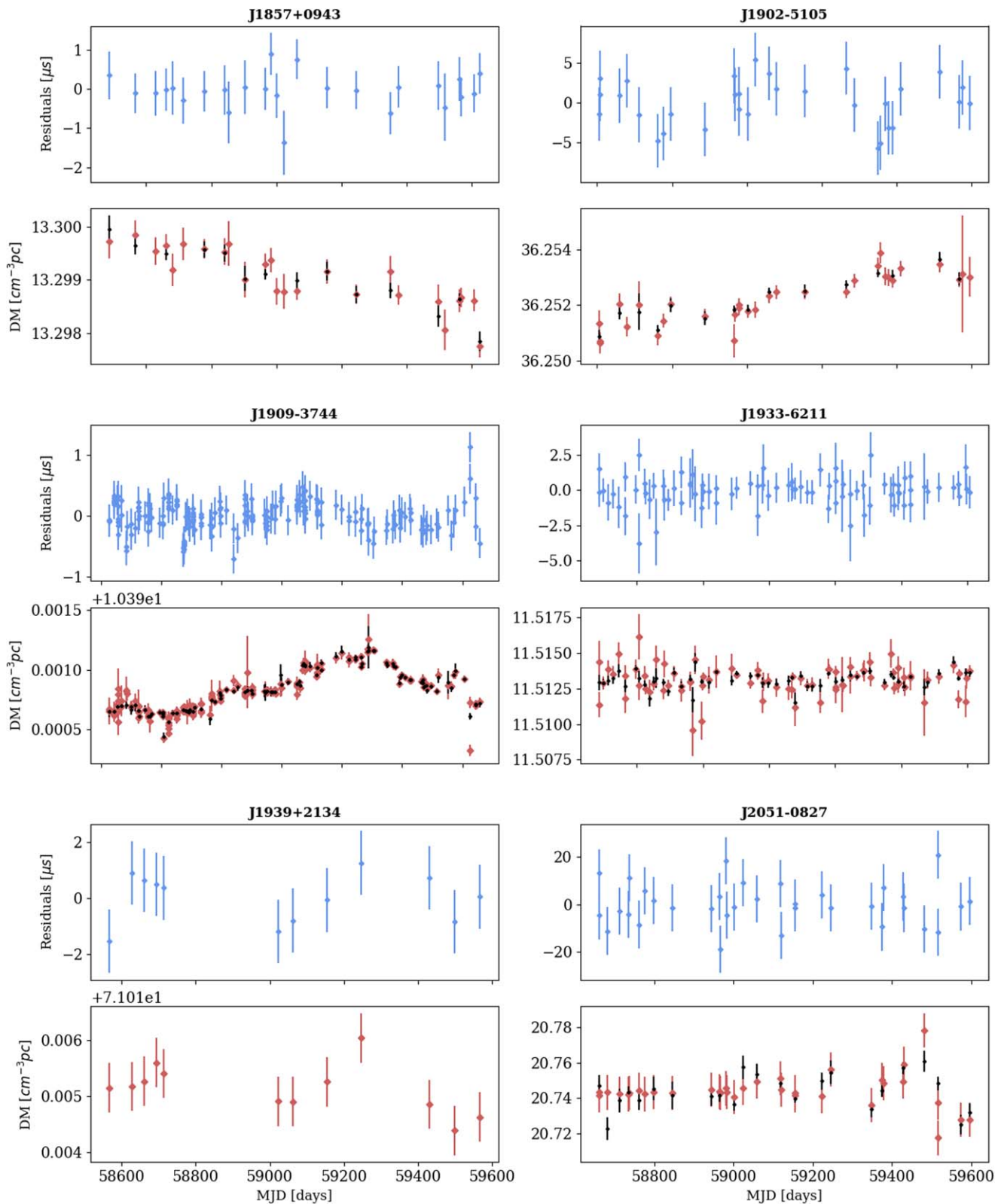
Figure 11. Timing residuals and DM variations for J1857+0943, J1902−5103, J1909−3744, J1933−6211, J1939+2134, and J2051−0827.
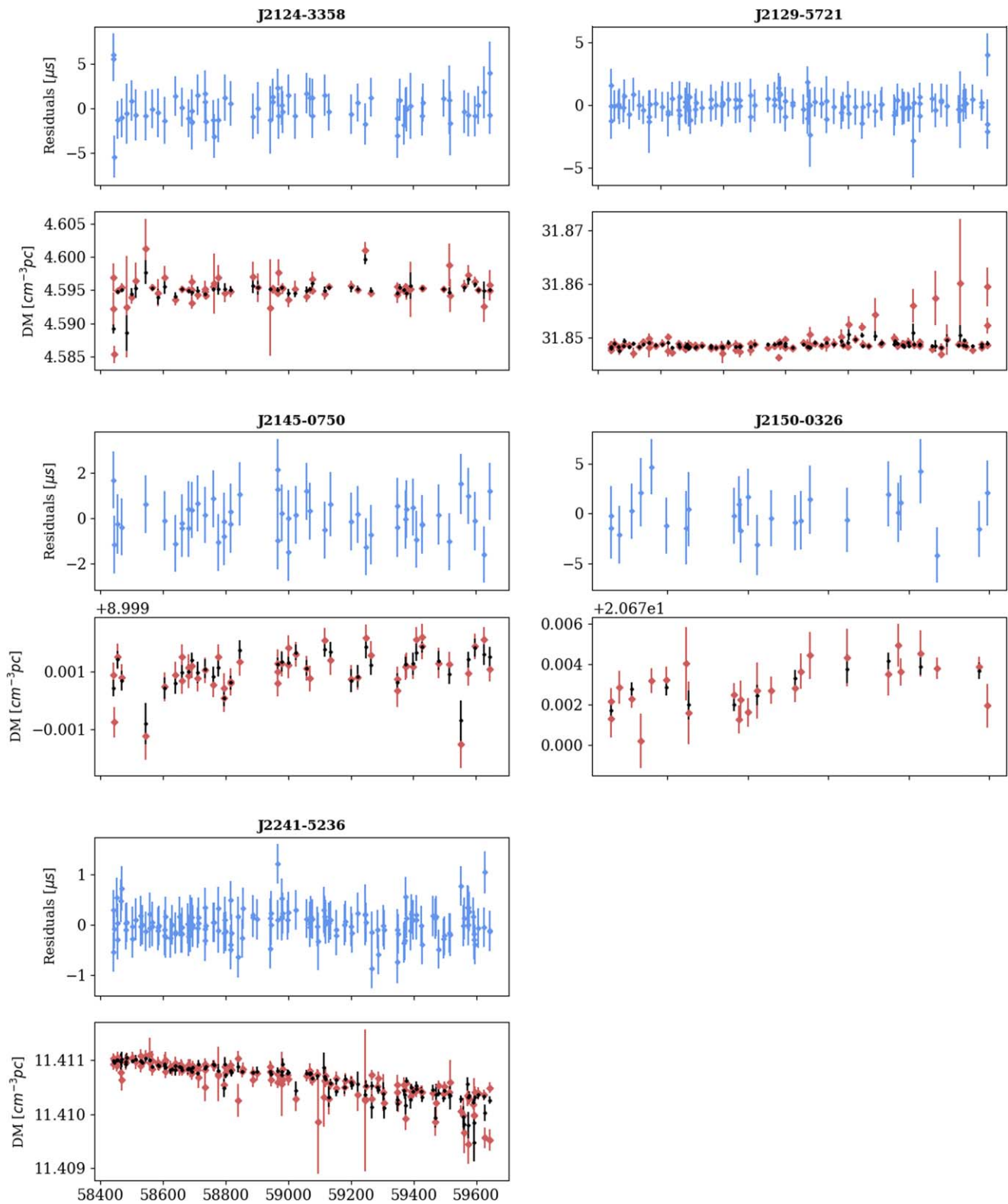
Figure 12. Timing residuals and DM variations for J2124−3358, J2129−5721, J2145−0750, J2150−0326, and J2241−5236.

Appendix B
Timing Parameters

Below we present Tables 2–8 with timing model parameters.

Table 2
Timing Parameters for J0030+0451, J0125−2327, J0348+0432, J0437−4715, and J0613−0200

	J0030+0451	J0125−2327	J0348+0432	J0437−4715	J0613−0200
MJD range	58486–59607	58480–59607	58486–59470	58441–59648	58441–59665
R.A. [hh:mm:ss]	00:30:27.4234(3)	01:25:1.074328(5)	03:48:43.64127(7)	04:37:16.0445973(9)	06:13:43.977048(3)
Decl. [dd:mm:ss]	04:51:39.726(10)	−23:27:8.1349(1)	04:32:11.462(2)	−47:15:9.99983(1)	−02:00:47.3405(1)
Proper motion in R.A. (mas yr^{-1})	−6.2100	37.14(8)	⋯	121.378(8)	1.84(4)
Proper motion in decl. (mas yr^{-1})	0.5000	10.5(2)	⋯	−71.42(1)	−10.6(1)
Spin frequency (s^{-1})	205.530698975007(4)	272.081088484952(1)	25.560636549613(1)	173.6879478266896(2)	326.6005667292508(8)
Spin frequency derivative (s^{-2})	−4.296(3) × 10^{-16}	−1.36332(10) × 10^{-15}	−1.5764(7) × 10^{-16}	−1.728459(8) × 10^{-15}	−1.02301(6) × 10^{-15}
DM (cm^{-3} pc)	4.332798	9.598062	40.466112	2.640302	38.779608
Parallax (mas)	2.7900	1.4(3)	⋯	6.3(3)	0.7(2)
Binary model	⋯	ELL1	ELL1	DDK	ELL1
Orbital period (days)	⋯	7.2771996382(8)	1.0242406060(5) × 10^{-1}	5.74104584368(9) × 10^{-0}	1.19851255685(5) × 10^{-0}
Projected semimajor axis (lt-s)	⋯	4.7297995(1)	0.140988(1)	3.36674563(2)	1.09144391(9)
Epoch of periastron (MJD)	⋯	⋯	⋯	59048.3754(6)	⋯
Longitude of periastron (deg)	⋯	⋯	⋯	1.54(4)	⋯
Eccentricity of orbit	⋯	⋯	⋯	0.00001920(1)	⋯
Epoch of ascending node (MJD)	⋯	59039.36296968(4)	58978.0641405(2)	⋯	59052.42591812(1)
First Laplace parameter	⋯	0.00000009(6)	−0.00009(3)	⋯	0.0000038(2)
Second Laplace parameter	⋯	0.00000053(5)	−0.00003(2)	⋯	0.0000032(2)
Time derivative of orbital period	⋯	⋯	⋯	⋯	⋯
Rate of advance of periastron	⋯	⋯	⋯	0.0137870	⋯
Rate of change of projected semimajor axis	⋯	⋯	⋯	⋯	⋯
Sine of inclination	⋯	⋯	⋯	⋯	⋯
Companion mass ($M_\odot$)	⋯	⋯	⋯	0.223972	⋯
Shapiro delay parameter h3 (μs)	⋯	⋯	⋯	⋯	⋯
Shapiro delay parameter h4 (μs)	⋯	⋯	⋯	⋯	⋯

Table 3
Timing Parameters for J0614−3329, J0711−6830, J0900−3144, J1017−7156, and J1022+1001

	J0614−3329	J0711−6830	J0900−3144	J1017−7156	J1022+1001
MJD range	58481−59596	58441−59664	58607−59595	58441−59664	58425−59665
R.A. [hh:mm:ss]	06:14:10.34823(2)	07:11:54.15385(1)	09:00:43.95220(2)	10:17:51.312124(8)	10:22:57.988(7)
Decl. [dd:mm:ss]	−33:29:54.1312(2)	−68:30:47.23742(8)	−31:44:30.8721(2)	−71:56:41.57562(3)	10:01:52.8(3)
Proper motion in R.A. (mas yr^{-1})	0.5800	−15.45(7)	−1.2(3)	−7.36(3)	−16.4260
Proper motion in decl. (mas yr^{-1})	−1.9200	14.08(7)	1.8(3)	6.83(3)	1.6741
Spin frequency (s^{-1})	317.594454701573(4)	182.1172372978466(7)	90.011843174693(1)	427.6219116054646(7)	60.7794488431391(8)
Spin frequency derivative (s^{-2})	$-1.7570(4) \times 10^{-15}$	$-4.9461(6) \times 10^{-16}$	$-3.958(1) \times 10^{-16}$	$-4.0508(6) \times 10^{-16}$	$-1.6017(8) \times 10^{-16}$
DM (cm^{-3} pc)	37.049000	18.406857	75.689026	94.223226	10.252000
Parallax (mas)	1.1000	⋯	1.8620	0.9(9)	1.5506
Binary model	ELL1	⋯	ELL1	ELL1H	ELL1H
Orbital period (days)	53.58461255(3)	⋯	18.737635770(5)	6.5118987118(2)	7.8051301640(10)
Projected semimajor axis (lt-s)	27.6387917(6)	⋯	17.2488093(5)	4.83004758(6)	16.7654220(6)
Epoch of periastron (MJD)	⋯	⋯	⋯	⋯	⋯
Longitude of periastron (deg)	⋯	⋯	⋯	⋯	⋯
Eccentricity of orbit	⋯	⋯	⋯	⋯	⋯
Epoch of ascending node (MJD)	59056.1281453(2)	⋯	59105.63920900(7)	59053.90652703(1)	59048.78549539(4)
First Laplace parameter	0.00004976(4)	⋯	0.00000986(4)	−0.00007136(2)	0.00009625(7)
Second Laplace parameter	0.00017382(4)	⋯	0.00000350(4)	0.00012288(2)	−0.00001333(8)
Time derivative of orbital period	⋯	⋯	⋯	⋯	⋯
Rate of advance of periastron	⋯	⋯	⋯	0.016(8)	0.0109124
Rate of change of projected semi-major axis	⋯	⋯	⋯	⋯	⋯
Sine of inclination	⋯	⋯	⋯	⋯	⋯
Companion mass ($M_\odot$)	0.240000	⋯	⋯	⋯	⋯
Shapiro delay parameter h3 (μs)	⋯	⋯	⋯	0.00000011(4)	0.0000011(4)
Shapiro delay parameter h4 (μs)	⋯	⋯	⋯	0.00000010(5)	0.0000004(5)

Table 4
Timing Parameters for J1024−0719, J1045−4509, J1125−6014, J1446−4701, and J1545−4550

	J1024−0719	J1045−4509	J1125−6014	J1446−4701	J1545−4550
MJD range	58443−59665	58454−59645	58442−59665	58443−59665	58442−59665
R.A. [hh:mm:ss]	10:24:38.64907(2)	10:45:50.17978(3)	11:25:55.242909(3)	14:46:35.70981(1)	15:45:55.945423(4)
Decl. [dd:mm:ss]	−07:19:19.9693(6)	−45:09:54.0569(3)	−60:14:6.80611(3)	−47:01:26.7964(2)	−45:50:37.50900(9)
Proper motion in R.A. (mas yr^{-1})	−35.3(3)	−5.9(3)	11.13(3)	−4.20(10)	−0.35(4)
Proper motion in decl. (mas yr^{-1})	−48.1(7)	4.4(3)	−13.04(3)	−2.8(2)	2.39(8)
Spin frequency (s^{-1})	193.715686208170(5)	133.793151505030(2)	380.1730997159584(5)	455.644022907970(2)	279.6977022449402(6)
Spin frequency derivative (s^{-2})	$-6.971(1) \times 10^{-16}$	$-3.165(2) \times 10^{-16}$	$-5.3938(3) \times 10^{-16}$	$-2.0362(2) \times 10^{-15}$	$-4.10347(4) \times 10^{-15}$
DM (cm^{-3} pc)	6.480135	58.150964	52.934539	55.830112	68.392666
Parallax (mas)	1.1(8)	3.3416	1.7(3)	0.4(5)	0.8(2)
Binary model	⋯	ELL1	ELL1	ELL1	ELL1H
Orbital period (days)	⋯	4.083529193(1)	8.7526035149(2)	$2.7766607312(9) \times 10^{-1}$	6.2030648297(3)
Projected semimajor axis (lt-s)	⋯	3.0151308(5)	8.3391936(5)	0.0640121(2)	3.84690438(9)
Epoch of periastron (MJD)	⋯	⋯	⋯	⋯	⋯
Longitude of periastron (deg)	⋯	⋯	⋯	⋯	⋯
Eccentricity of orbit	⋯	⋯	⋯	⋯	⋯
Epoch of ascending node (MJD)	⋯	59049.0111262(1)	59053.335201025(8)	59053.9339604(1)	59056.49624717(2)
First Laplace parameter	⋯	−0.0000205(4)	−0.00000002(3)	0.000003(6)	−0.00000871(5)
Second Laplace parameter	⋯	−0.0000104(4)	−0.00000064(1)	0.000010(6)	−0.00000968(4)
Time derivative of orbital period	⋯	⋯	⋯	⋯	⋯
Rate of advance of periastron	⋯	⋯	⋯	⋯	⋯
Rate of change of projected semimajor axis	⋯	⋯	⋯	⋯	⋯
Sine of inclination	⋯	⋯	0.977(7)	⋯	⋯
Companion mass ($M_\odot$)	⋯	⋯	0.33(5)	⋯	⋯
Shapiro delay parameter h3 (μs)	⋯	⋯	⋯	⋯	0.00000007(6)
Shapiro delay parameter h4 (μs)	⋯	⋯	⋯	⋯	−0.00000010(9)

Table 5
Timing Parameters for J1600-3053, J1603-7202, J1643-1224, J1713+0747 and J1730-2304

	J1600−3053	J1603−7202	J1643−1224	J1713+0747	J1730−2304
MJD range	58443−59665	58443−59664	58454−59664	58426−59265	58455−59664
R.A. [hh:mm:ss]	16:00:51.902531(5)	16:03:35.67088(3)	16:43:38.16602(2)	17:13:49.536688(5)	17:30:21.6849(3)
Decl. [dd:mm:ss]	−30:53:49.4528(2)	−72:02:32.8216(2)	−12:24:58.633(1)	07:47:37.4514(1)	−23:04:31.12(7)
Proper motion in R.A. (mas yr^{-1})	−0.77(6)	−2.4(1)	5.9(2)	4.7(1)	20.0246
Proper motion in decl. (mas yr^{-1})	−6.8(2)	−7.2(2)	1.9(10)	−3.9(4)	−4.9776
Spin frequency (s^{-1})	277.9377110420382(7)	67.3765821486238(5)	216.373340194411(2)	218.811843674173(2)	123.110288948911(1)
Spin frequency derivative (s^{-2})	−7.3383(5) × 10^{-16}	−7.092(4) × 10^{-17}	−8.645(2) × 10^{-16}	−4.086(3) × 10^{-16}	−3.060(1) × 10^{-16}
DM (cm^{-3} pc)	52.328259	38.042070	62.301899	15.917131	9.622926
Parallax (mas)	1.0(2)	0.7019	2.6(8)	0.0(4)	1.7(8)
Binary model	ELL1H	ELL1	DD	DDK	...
Orbital period (days)	14.3484575522(8)	6.3086295734(7)	147.0173956(1)	67.82512992(2)	...
Projected semimajor axis (lt-s)	8.8016553(1)	6.8806683(3)	25.0725735(5)	32.3424220(1)	...
Epoch of periastron (MJD)	...	...	58987.082(2)	58847.926(1)	...
Longitude of periastron (deg)	...	...	321.849(4)	176.240(6)	...
Eccentricity of orbit	...	...	0.00050576(3)	0.000074955(9)	...
Epoch of ascending node (MJD)	59056.37152772(2)	59050.18353655(4)	...	...	...
First Laplace parameter	−0.00000546(2)	0.00000160(8)	...	...	...
Second Laplace parameter	−0.00017365(2)	−0.00000925(7)	...	...	...
Time derivative of orbital period	...	...	...	...	...
Rate of advance of periastron	−0.007(8)	...	...	...	...
Rate of change of projected semimajor axis	...	...	−0.04(1)	...	...
Sine of inclination	...	...	...	...	...
Companion mass ($M_\odot$)	...	...	...	0.538032	...
Shapiro delay parameter h3 (μs)	0.00000032(7)	...	...	...	...
Shapiro delay parameter h4 (μs)	0.00000011(10)	...	...	...	...

Table 6
Timing Parameters for J1741+1351, J1744−1134, J1824−2452A, J1832−0836, and J1857+0943

	J1741+1351	J1744−1134	J1824−2452A	J1832−0836	J1857+0943
MJD range	58627−59571	58442−59658	58627−59664	58627−59607	58486−59624
R.A. [hh:mm:ss]	17:41:31.13983(1)	17:44:29.421749(3)	18:24:32.0076(2)	18:32:27.589563(5)	18:57:36.388636(7)
Decl. [dd:mm:ss]	13:51:44.0624(3)	−11:34:54.7976(2)	−24:52:10.94(5)	−08:36:55.1437(3)	09:43:17.1470(2)
Proper motion in R.A. (mas yr^{-1})	−8.7609	18.86(4)	−0.2339	−8.13(8)	−2.6(1)
Proper motion in decl. (mas yr^{-1})	−6.5447	−9.5(2)	−8.9459	−21.2(4)	−5.9(2)
Spin frequency (s^{-1})	266.869166434737(3)	245.4261233068814(5)	327.40552589863(2)	367.767120938621(2)	186.494081052219(1)
Spin frequency derivative (s^{-2})	−2.1524(2) × 10^{-15}	−5.3818(4) × 10^{-16}	−1.73531(2) × 10^{-13}	−1.1194(2) × 10^{-15}	−6.2038(8) × 10^{-16}
DM (cm^{-3} pc)	24.198581	3.139444	119.902567	28.195970	13.298525
Parallax (mas)	0.4586	3.1(2)	−0.2430	1.1(3)	1.6(5)
Binary model	ELL1	...	...	...	ELL1
Orbital period (days)	16.335347843(6)	...	...	...	12.32717119165031
Projected semimajor axis (lt-s)	11.0033142(4)	...	...	...	9.230780241
Epoch of periastron (MJD)	...	...	...	...	...
Longitude of periastron (deg)	...	...	...	...	...
Eccentricity of orbit	...	...	...	...	...
Epoch of ascending node (MJD)	59102.65959876(9)	...	...	...	59058.66451258(5)
First Laplace parameter	−0.00000399(8)	...	...	...	−0.0000215720
Second Laplace parameter	−0.00000896(7)	...	...	...	0.0000024568
Time derivative of orbital period	...	...	...	...	...
Rate of advance of periastron	...	...	...	...	...
Rate of change of projected semimajor axis	...	...	...	...	...
Sine of inclination	0.941114	...	...	...	0.9990(4)
Companion mass ($M_\odot$)	0.254703	...	...	...	0.253681
Shapiro delay parameter h3 (μs)	...	...	...	...	...
Shapiro delay parameter h4 (μs)	...	...	...	...	...

Table 7
Timing Parameters for J1902−5105, J1909−3744, J1933−6211, J1939+2134, and J2051−0827

	J1902−5105	J1909−3744	J1933−6211	J1939+2134	J2051−0827
MJD range	58604−59595	58427−59658	58485−59607	58566−59567	58659−59596
R.A. [hh:mm:ss]	19:02:2.84424(4)	19:09:47.424713(1)	19:33:32.41353(2)	19:39:38.56131(2)	20:51:7.5244(4)
Decl. [dd:mm:ss]	−51:05:57.0563(9)	−37:44:14.91222(5)	−62:11:46.6962(2)	21:34:59.1205(3)	−08:27:37.76(2)
Proper motion in R.A. (mas yr^{-1})	−3.0375	−9.49(1)	−5.4(2)	0.0610	6.4920
Proper motion in decl. (mas yr^{-1})	−11.1896	−35.72(5)	11.2(2)	−0.4044	0.8409
Spin frequency (s^{-1})	573.92104402934(2)	339.3156919155664(2)	282.212317830028(2)	641.92821931762(1)	221.79628690412(4)
Spin frequency derivative (s^{-2})	$-3.035(1) \times 10^{-15}$	$-1.61469(2) \times 10^{-15}$	$-3.078(2) \times 10^{-16}$	$-4.33064(7) \times 10^{-14}$	$-6.36(4) \times 10^{-16}$
DM (cm^{-3} pc)	36.250000	10.391734	11.499000	71.014000	20.729900
Parallax (mas)	⋯	1.26(5)	⋯	0.2368	⋯
Binary model	ELL1	ELL1	ELL1	⋯	ELL1
Orbital period (days)	2.011803739(1)	$1.53344945354(2) \times 10^{-0}$	12.819406522(2)	⋯	0.0991102480(6)
Projected semimajor axis (lt-s)	1.901956478	1.89799100(10)	12.2815798(3)	⋯	0.045075(4)
Epoch of periastron (MJD)	⋯	⋯	⋯	⋯	⋯
Longitude of periastron (deg)	⋯	⋯	⋯	⋯	⋯
Eccentricity of orbit	⋯	⋯	⋯	⋯	⋯
Epoch of ascending node (MJD)	59099.3814765(2)	59042.266169044(4)	59051.25497668(4)	⋯	59127.024438(2)
First Laplace parameter	0.0000000000	0.00000007(5)	0.00000135(4)	⋯	0.0000000000
Second Laplace parameter	0.0000000000	−0.00000007(3)	−0.00000029(4)	⋯	0.0000000000
Time derivative of orbital period	⋯	⋯	⋯	⋯	⋯
Rate of advance of periastron	⋯	⋯	⋯	⋯	⋯
Rate of change of projected semimajor axis	⋯	⋯	⋯	⋯	⋯
Sine of inclination	⋯	0.9983(3)	⋯	⋯	⋯
Companion mass ($M_\odot$)	⋯	0.202(6)	⋯	⋯	⋯
Shapiro delay parameter h3 (μs)	⋯	⋯	⋯	⋯	⋯
Shapiro delay parameter h4 (μs)	⋯	⋯	⋯	⋯	⋯

Table 8
Timing Parameters J2124−3358, J2129−5721, J2145−0750, J2150−0326, and J2241−5236

	J2124−3358	J2129−5721	J2145−0750	J2150−0326	J2241−5236
MJD range	58441−59645	58441−59645	58441−59645	58659−59595	58441−59644
R.A. [hh:mm:ss]	21:24:43.83534(4)	21:29:22.78125(3)	21:45:50.45355(5)	21:50:27.23531(10)	22:41:42.039596(4)
Decl. [dd:mm:ss]	−33:58:45.4778(9)	−57:21:14.3313(3)	−07:50:18.589(2)	−03:26:32.832(4)	−52:36:36.27108(4)
Proper motion in R.A. (mas yr^{-1})	−13.9(4)	9.3(2)	−10.3(8)	⋯	18.75(3)
Proper motion in decl. (mas yr^{-1})	−49.8(8)	−9.7(3)	−7(2)	⋯	−5.17(5)
Spin frequency (s^{-1})	202.793896594889(3)	268.359230930218(3)	62.2958887629109(7)	284.84324670257(1)	457.3101563491688(8)
Spin frequency derivative (s^{-2})	$-8.463(2) \times 10^{-16}$	$-1.5019(2) \times 10^{-15}$	$-1.1563(5) \times 10^{-16}$	$-6.622(9) \times 10^{-16}$	$-1.44219(6) \times 10^{-15}$
DM (cm^{-3} pc)	4.592633	31.846624	9.002578	20.670000	11.410342
Parallax (mas)	3(1)	0.4232	3.4(7)	⋯	1.2(2)
Binary model	⋯	ELL1	ELL1	ELL1	ELL1
Orbital period (days)	⋯	6.625492997(2)	6.8389025093(9)	4.044550594(3)	$1.4567223817(2) \times 10^{-1}$
Projected semimajor axis (lt-s)	⋯	3.5005689(4)	10.1641111(4)	3.320713(1)	0.02579534(6)
Epoch of periastron (MJD)	⋯	⋯	⋯	⋯	⋯
Longitude of periastron (deg)	⋯	⋯	⋯	⋯	⋯
Eccentricity of orbit	⋯	⋯	⋯	⋯	⋯
Epoch of ascending node (MJD)	⋯	59042.5329168(1)	59043.17563464(5)	59128.4793005(3)	59041.98680351(6)
First Laplace parameter	⋯	−0.0000043(2)	−0.00000691(8)	0.0000033(6)	−0.000004(5)
Second Laplace parameter	⋯	−0.0000118(2)	−0.00001808(7)	0.0000112(7)	−0.000003(5)
Time derivative of orbital period	⋯	⋯	⋯	⋯	⋯
Rate of advance of periastron	⋯	⋯	0.0242437	⋯	⋯
Rate of change of projected semimajor axis	⋯	⋯	⋯	⋯	⋯
Sine of inclination	⋯	⋯	⋯	⋯	⋯
Companion mass ($M_\odot$)	⋯	⋯	⋯	⋯	⋯
Shapiro delay parameter h3 (μs)	⋯	⋯	⋯	⋯	⋯
Shapiro delay parameter h4 (μs)	⋯	⋯	⋯	⋯	⋯

Curyło et al.

ORCID iDs

Małgorzata Curyło https://orcid.org/0000-0002-7031-4828
Timothy T. Pennucci https://orcid.org/0000-0001-5465-2889
Matthew Bailes https://orcid.org/0000-0003-3294-3081
N. D. Ramesh Bhat https://orcid.org/0000-0002-8383-5059
Andrew D. Cameron https://orcid.org/0000-0002-2037-4216
Shi Dai https://orcid.org/0000-0002-9618-2499
Richard N. Manchester https://orcid.org/0000-0001-9445-5732
Rami Mandow https://orcid.org/0000-0001-5131-522X
Matthew T. Miles https://orcid.org/0000-0002-5455-3474
Daniel J. Reardon https://orcid.org/0000-0002-2035-4688
Ryan M. Shannon https://orcid.org/0000-0002-7285-6348
Renée Spiewak https://orcid.org/0000-0002-6730-3298
Willem van Straten https://orcid.org/0000-0003-2519-7375
Xing-Jiang Zhu https://orcid.org/0000-0001-7049-6468
Andrew Zic https://orcid.org/0000-0002-9583-2947

References

Alam, M. F., Arzoumanian, Z., Baker, P. T., et al. 2021a, ApJS, 252, 4
Alam, M. F., Arzoumanian, Z., Baker, P. T., et al. 2021b, ApJS, 252, 5
Amiri, M., Bandura, K., Boskovic, A., et al. 2022, ApJS, 261, 29
Amiri, M., Bandura, K. M., Boyle, P. J., et al. 2021, ApJS, 255, 5
Bulatek, A., & White, S. 2020, AAS Meeting, 235, 175.17
Burke-Spolaor, S., Taylor, S. R., Charisi, M., et al. 2019, A&ARv, 27, 5
Cordes, J. M., Shannon, R. M., & Stinebring, D. R. 2016, ApJ, 817, 16
Damour, T., & Taylor, J. H. 1992, PhRv, 45, 1840
Desvignes, G., Caballero, R. N., Lentati, L., et al. 2016, MNRAS, 458, 3341
Ellis, J. A., Vallisneri, M., Taylor, S. R., & Baker, P. T. 2019, ENTERPRISE: Enhanced Numerical Toolbox Enabling a Robust PulsaR Inference SuitE, Astrophysics Source Code Library, ascl:1912.015
Fonseca, E., Cromartie, H. T., Pennucci, T. T., et al. 2021, ApJL, 915, L12
Freire, P. C. C., & Wex, N. 2010, MNRAS, 409, 199
Goncharov, B., Reardon, D. J., Shannon, R. M., et al. 2021, MNRAS, 502, 478
Graikou, E., Verbiest, J. P. W., Osłowski, S., et al. 2017, MNRAS, 471, 4579
Hassall, T. E., Stappers, B. W., Hessels, J. W. T., et al. 2012, A&A, 543, A66
Helfand, D. J., Manchester, R. N., & Taylor, J. H. 1975, ApJ, 198, 661
Hobbs, G. 2013, CQGra, 30, 224007
Hobbs, G., Dai, S., Manchester, R. N., et al. 2019, RAA, 19, 020
Hobbs, G., Manchester, R. N., Dunning, A., et al. 2020, PASA, 37, e012
Hobbs, G. B., Edwards, R. T., & Manchester, R. N. 2006, MNRAS, 369, 655
Hotan, A. W., Bailes, M., & Ord, S. M. 2006, MNRAS, 369, 1502
Hotan, A. W., van Straten, W., & Manchester, R. N. 2004, PASA, 21, 302
Kaur, D., Ramesh Bhat, N. D., Dai, S., et al. 2022, ApJL, 930, L27
Kerr, M., Reardon, D. J., Hobbs, G., et al. 2020, PASA, 37, e020
Kopeikin, S. M. 1995, ApJL, 439, L5
Kopeikin, S. M. 1996, ApJL, 467, L93
Kramer, M., Menten, K., Barr, E. D., et al. 2016, in MeerKAT Science: On the Pathway to the SKA, The MeerKAT Max-Planck S-band System, 3
Lange, C., Camilo, F., Wex, N., et al. 2001, MNRAS, 326, 274
Lee, K. J. 2016, in ASP Conf. Ser. 502, Frontiers in Radio Astronomy and FAST Early Sciences Symp. 2015, ed. L. Qain & D. Li (San Francisco, CA: ASP), 19
Liu, K., Desvignes, G., Cognard, I., et al. 2014, MNRAS, 443, 3752
Lorimer, D. R., & Kramer, M. 2004, Handbook of Pulsar Astronomy, Vol. 4 (Cambridge: Cambridge Univ. Press)
Luo, J., Ransom, S., Demorest, P., et al. 2021, ApJ, 911, 45
Manchester, R. N. & IPTA 2013, CQGra, 30, 224010
McLaughlin, M. A. 2013, CQGra, 30, 224008
Miles, M. T., Shannon, R. M., Bailes, M., et al. 2023, MNRAS, 519, 3976
Nice, D., Demorest, P., Stairs, I., et al. 2015, Tempo: Pulsar timing data analysis, Astrophysics Source Code Library, ascl:1509.002
Nobleson, K., Agarwal, N., Girgaonkar, R., et al. 2022, MNRAS, 512, 1234
Padmanabh, P. V., Barr, E. D., Champion, D. J., et al. 2021, MNRAS, 500, 1178
Parthasarathy, A., Bailes, M., Shannon, R. M., et al. 2021, MNRAS, 502, 407
Paul, A., M. A, K., Dey, L., et al. 2019, in URSI Asia-Pacific Radio Science Conf. (AP-RASC), The Indian Pulsar Timing Array (InPTA) (Piscataway, NJ: IEEE), 1
Pennucci, T. T. 2019, ApJ, 871, 34
Pennucci, T. T., Demorest, P. B., & Ransom, S. M. 2014, ApJ, 790, 93
Pennucci, T. T., Demorest, P. B., & Ransom, S. M. 2016, Pulse Portraiture: Pulsar Timing, Astrophysics Source Code Library, ascl:1606.013
Ramachandran, R., & Kramer, M. 2003, A&A, 407, 1085
Reardon, D. J., Shannon, R. M., Cameron, A. D., et al. 2021, MNRAS, 507, 2137
Shannon, R. M., & Cordes, J. M. 2010, ApJ, 725, 1607
Shannon, R. M., Osłowski, S., Dai, S., et al. 2014, MNRAS, 443, 1463
Shao, M., & You, X. P. 2016, AcASn, 57, 517
Sharma, S. S., Roy, J., Bhattacharyya, B., et al. 2022, ApJ, 936, 86
Spiewak, R., Bailes, M., Miles, M. T., et al. 2022, PASA, 39, 27
Stovall, K., Lynch, R. S., Ransom, S. M., et al. 2014, ApJ, 791, 67
Tarafdar, P., Nobleson, K., Rana, P., et al. 2022, PASA, 39, e053
Vallisneri, M., Taylor, S. R., Simon, J., et al. 2020, ApJ, 893, 112
van Straten, W. 2013, ApJS, 204, 13
van Straten, W., & Bailes, M. 2011, PASA, 28, 1
van Straten, W., Bailes, M., Britton, M., et al. 2001, Natur, 412, 158